The Astrophysical Journal, 964:74 (29pp), 2024 March 20 https://doi.org/10.3847/1538-4357/ad2704

ULTRASAT: A Wide-field Time-domain UV Space Telescope

Y. Shvartzvald[1], E. Waxman[1], A. Gal-Yam[1], E. O. Ofek[1], S. Ben-Ami[1], D. Berge[2,3], M. Kowalski[2,3], R. Bühler[2], S. Worm[2], J. E. Rhoads[4], I. Arcavi[5,6], D. Maoz[5], D. Polishook[7], N. Stone[8], B. Trakhtenbrot[5], M. Ackermann[2], O. Aharonson[9,10], O. Birnholtz[11], D. Chelouche[12,13], D. Guetta[14], N. Hallakoun[1], A. Horesh[8], D. Kushnir[1], T. Mazeh[5], J. Nordin[3], A. Ofir[9], S. Ohm[2], D. Parsons[2], A. Pe'er[11], H. B. Perets[15,16], V. Perdelwitz[9], D. Poznanski[5], I. Sadeh[2], I. Sagiv[17], S. Shahaf[1], M. Soumagnac[11], L. Tal-Or[14,18], J. Van Santen[2], B. Zackay[1], O. Guttman[1], P. Rekhi[1], A. Townsend[3], A. Weinstein[19], and I. Wold[4]
[1] Department of Particle Physics and Astrophysics, Weizmann Institute of Science, Rehovot 7610001, Israel; yossi.shvartzvald@weizmann.ac.il
[2] Deutsches Elektronen Synchrotron DESY, Platanenallee 6, 15738 Zeuthen, Germany
[3] Institut fur Physik, Humboldt-Universitzäu Berlin, D-12489 Berlin, Germany
[4] NASA Goddard Space Flight Center, Greenbelt, MD 20771, USA
[5] School of Physics and Astronomy, Tel-Aviv University, Tel-Aviv 69978, Israel
[6] CIFAR Azrieli Global Scholars program, CIFAR, Toronto, Canada
[7] Faculty of Physics, Weizmann Institute of Science, Rehovot 7610001, Israel
[8] Racah Institute of Physics, The Hebrew University of Jerusalem, Jerusalem 91904, Israel
[9] Helen Kimmel Center for Planetary Science, Weizmann Institute of Science, Rehovot, Israel
[10] Planetary Science Institute, Tucson, AZ, USA
[11] Department of Physics, Bar-Ilan University, Ramat-Gan 52900, Israel
[12] Department of Physics, Faculty of Natural Sciences, University of Haifa, Haifa 3498838, Israel
[13] Haifa Research Center for Theoretical Physics and Astrophysics, University of Haifa, Haifa 3498838, Israel
[14] Department of Physics, Ariel University, Ariel, IL-40700, Israel
[15] Physics Department, Technion—Israel Institute of Technology, Technion City, Haifa 3200002, Israel
[16] Department of Natural Sciences, The Open University of Israel, 1 University Road, P.O. Box 808, Raanana 4353701, Israel
[17] ElOp—Elbit Systems Ltd., Rehovot, Israel
[18] Astrophysics Geophysics And Space Science Research Center, Ariel University, Ariel 40700, Israel
[19] Tufts University, Medford, MA 02155, USA
Received 2023 April 27; revised 2024 January 29; accepted 2024 February 5; published 2024 March 18

Abstract

The Ultraviolet Transient Astronomy Satellite (ULTRASAT) is scheduled to be launched to geostationary orbit in 2027. It will carry a telescope with an unprecedentedly large field of view (204 deg^2) and near-ultraviolet (NUV; 230–290 nm) sensitivity (22.5 mag, 5σ, at 900 s). ULTRASAT will conduct the first wide-field survey of transient and variable NUV sources and will revolutionize our ability to study the hot transient Universe. It will explore a new parameter space in energy and timescale (months-long light curves with minutes cadence), with an extragalactic volume accessible for the discovery of transient sources that is >300 times larger than that of the Galaxy Evolution Explorer (GALEX) and comparable to that of the Vera Rubin Observatory's Legacy Survey of Space and Time. ULTRASAT data will be transmitted to the ground in real time, and transient alerts will be distributed to the community in <15 minutes, enabling vigorous ground-based follow up of ULTRASAT sources. ULTRASAT will also provide an all-sky NUV image to >23.5 AB mag, over 10 times deeper than the GALEX map. Two key science goals of ULTRASAT are the study of mergers of binaries involving neutron stars, and supernovae. With a large fraction (>50%) of the sky instantaneously accessible, fast (minutes) slewing capability, and a field of view that covers the error ellipses expected from gravitational-wave (GW) detectors beyond 2026, ULTRASAT will rapidly detect the electromagnetic emission following binary neutron star/neutron star–black hole mergers identified by GW detectors, and will provide continuous NUV light curves of the events. ULTRASAT will provide early (hour) detection and continuous high-cadence (minutes) NUV light curves for hundreds of core-collapse supernovae, including for rarer supernova progenitor types.

Unified Astronomy Thesaurus concepts: Near ultraviolet astronomy (1094); Space telescopes (1547); Time domain astronomy (2109); Gravitational wave sources (677); Supernovae (1668); Gamma-ray bursts (629); Cosmology (343); Exoplanets (498); Active galactic nuclei (16); Tidal disruption (1696); Galaxies (573); Solar system astronomy (1529)

1. Introduction

Time domain surveys are a developing focus of astronomy with an unusual discovery potential. There are three main reasons for this. First, the static sky has already been well imaged in most electromagnetic (EM) bands. Second, new technology enables efficient monitoring of large swaths of sky. Finally, some of the most exciting frontiers, particularly those related to cosmic cataclysms, require wide-field synoptic surveys. It is therefore not surprising that large powerful surveys across the EM spectrum (e.g., the Square Kilometre Array, Vera Rubin Observatory (Rubin)'s Legacy Survey of Space and Time (LSST), the Zwicky Transient Facility (ZTF), eROSITA, Euclid, and Roman) are at the focus of attention by the global community. However, a key piece, the UV, is missing from this synoptic suite.

The UV band is unique in its ability to probe the physics of hot sources (Sagiv et al. 2014; Kulkarni et al. 2021). Many of

Table 1
ULTRASAT Key Properties

Property	Value	Comments
Spacecraft parameters		
Orbit	GEO	…
Real-time download of data	Continuous	…
Slew rate	>30° minute^{-1}	…
Transient alert after observation end	<15 minutes	For both survey and target-of-opportunity (ToO) modes
Sky accessibility at any given moment	>50%	See Figure 3
Observation start after ToO trigger	<15 minutes	At any visible position
Payload parameters		
Aperture	33 cm	…
Total FOV	204 deg^2	Covered by four 7.°14 × 7.°14 sensors
Pixel scale	5.″4 pixel^{-1}	Total of 89.9M pixels
Operation wave band	230–290 nm	See Figure 4
Mean throughput in operation wave band	0.25	See Figure 4
Out-of-band rejection (>300 nm)	2.9×10^{-5}	See Figure 4
Mean effective FWHM[a]	8.″3	See Figure 5
Mean limiting magnitude[a] (in 900 s, 5σ)	22.5 AB mag	See Figure 6

Note.
[a] In central 170 deg^2 of FOV, for a $T = 20{,}000$ K blackbody source. Assuming the conservative background values as in Table 3.

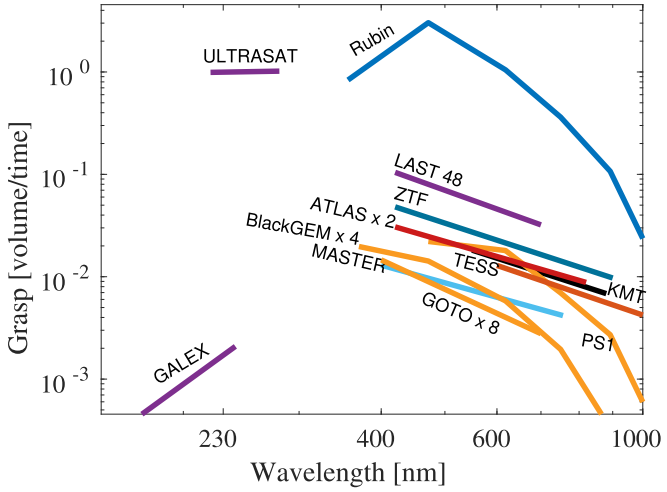

Figure 1. The volume of the universe per unit time (grasp; Ofek & Ben-Ami 2020) accessible to several past, current, and future sky surveys (Rubin/LSST, Ivezić et al. 2019; LAST, Ofek et al. 2023a; ZTF, Bellm et al. 2019; ATLAS, Heinze et al. 2018; Pan-STARRS, Chambers et al. 2016; KMTNet, Kim et al. 2016; TESS, Ricker et al. 2015; Black-GEM, Bloemen et al. 2015; MASTER, Gorbovskoy et al. 2013; GOTO, Steeghs et al. 2022; and GALEX, Martin et al. 2005), as a function of wavelength (normalized such that ULTRASAT's grasp is 1). The grasp is given for a 20,000 K blackbody source spectrum (e.g., a hot transient). ULTRASAT's grasp is an order of magnitude larger than that of current surveys, 2 orders of magnitudes larger than that of GALEX, the largest grasp UV mission to date, and comparable to that of LSST, the largest grasp optical survey under construction.

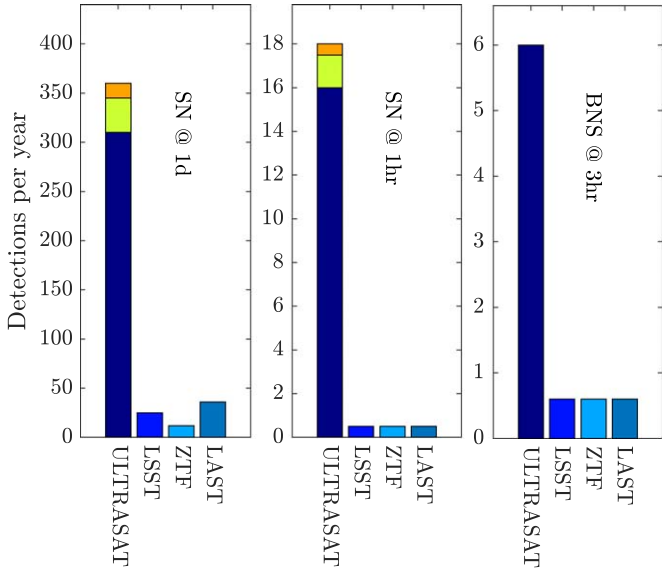

Figure 2. The number per year of supernova (SN) transients and EM transients following binary neutron star (BNS) mergers, expected to be detected at early time (as indicated in the plot) by ULTRASAT (assuming the limiting magnitude for 3 × 300 s exposures), Rubin (LSST; Ivezić et al. 2019), ZTF (Bellm et al. 2019), and LAST (Ofek & Ben-Ami 2020). The blue/green/orange parts of the SN bars correspond to red supergiant (RSG)/blue supergiant (BSG)/Wolf–Rayet (W-R) progenitors, respectively. The SN rates are taken from Ganot et al. (2016), based on simulations calibrated to GALEX/Palomar Transient Factory observations. The BNS rates were obtained assuming 12 gravitational-wave (GW) detections per year out to 300 Mpc, with UV flux similar to that observed following GW170817.

the interesting and exotic astrophysical sources shine brightly in the UV, and explosive transients are initially hot, so UV can provide the earliest notification. Thus, even a modest UV time-domain explorer has a vast discovery potential, and can uncover evidence to solve many open questions.

The Ultraviolet Transient Astronomy Satellite (ULTRASAT) is a UV space telescope that will undertake the first wide-field UV time-domain survey, and is planned to be launched to its geostationary orbit (GEO) in 2027. Its main properties are given in Table 1. The celestial volume accessible for transient detection by a survey, and hence the number of extragalactic objects detected per unit time, are proportional to the survey's grasp $G \propto \Omega S_m^{-3/2}$, where Ω is the field of view (FOV) and S_m is the minimum detectable flux (Ofek & Ben-Ami 2020). Figure 1 shows a comparison of the grasp for hot transients of ULTRASAT with that of other surveys. ULTRASAT's grasp is much larger than that of existing optical surveys, comparable to

Table 2
ULTRASAT Science Highlights

Source Type	# Events per 3 yr mission	Science Impact
SNe (Sections 5.2 and 5.3)		
Shock breakout and early (shock cooling) of core-collapse SNe	>40 >500	Understand the explosive death of massive stars
Superluminous supernovae (SLSNe)	>250	Early evolution, shock-cooling emission
Type Ia SNe	>1000	Discriminate between single-degenerate (SD) and double-degenerate (DD) progenitors, dust reddening
Compact object transients (Sections 5.1 and 5.7)		
Emission from GW events: NS–NS and NS–BH	~25	Constrain the physics of the sources of GWs
Tidal disruption events (TDEs)	>300 (high cadence) >4500 (low cadence)	Accretion physics, BH demographics
Quasars and active galactic nuclei (AGNs; Section 5.8)		
Continuous UV light curves	>7500	Accretion physics, broad-line region (BLR) reverberation mapping (RM), lensed quasars
AGN-related flares and transients	>100	Accretion physics
Stars and exoplanets (Sections 5.5 and 5.6)		
Active and flaring stars	$>4 \times 10^5$	Planet habitability, high-energy flare frequency, stellar magnetic structure, gyrochronology, magnetospheres
White dwarfs (WDs)	$>3 \times 10^4$	Planetary systems, debris accretion, rotation-related variability
RR Lyrae	>1000	Pulsation physics
Nonradial hot pulsators, e.g., α Cyg, δ Scuti, SX Phe, and β Cep types	>250	Asteroseismology
Eclipsing binaries	>400	Chromosphere and eclipse mapping
Galaxies and clusters (Section 5.9)		
All-sky survey: galaxies	$>10^8$	Galaxy evolution, star formation rate
GRBs (Section 5.4)		
GRBs occurring in field	~30	Prompt emission and afterglow physics, dust reddening
Orphan afterglows	>30	Fireball Γ and opening angle distributions
Solar system (Section 5.10)		
Asteroids and other small bodies	$>10^4$	Asteroid classification, origin

that of Rubin, which is planned to begin operation in 2024, and over 300 times that of the Galaxy Evolution Explorer (GALEX), which had a similar sensitivity but a much smaller FOV. The large grasp, continuous cadence, and fast slew rate enable early detection of transients by ULTRASAT at a rate that is much larger than that of existing and planned surveys, as demonstrated in Figure 2. In addition to its large grasp, ULTRASAT is unique in its energy and time windows. It will provide continuous months-long UV light curves with minutes cadence, as well as early alerts that will enable rapid ground- and space-based follow up of transients. Historically, such great leaps in capability have led to marvelous discoveries—a major incentive for ULTRASAT.

While ULTRASAT is expected to revolutionize the study of a wide range of transients (see Section 5 and Table 2), the mission design is set by two key science goals of fundamental importance—the study of the mergers of binaries involving neutron stars (BNS, or neutron star–black hole (NS–BH) binaries; see Section 5.1) and the study of SNe (see Section 5.2). Measuring the EM emission following BNS/NS–BH mergers will (i) provide direct constraints on the structure and composition of the ejected material, thus providing unique diagnostics of the properties of matter at nuclear density and of the merger dynamics; (ii) enable determinations of whether mergers are the sources of *r*-process elements and gamma-ray bursts (GRBs); and (iii) allow determinations of the location in, and properties of, the host galaxy, thus revealing the stellar antecedents of the binary systems. Measuring the early shock breakout/cooling part of SN light curves will provide unique information on the progenitor star and its preexplosion evolution, in particular mapping the different types of SNe to the different stellar progenitors, and hence also providing constraints on the explosion mechanisms, which are not fully understood.

Rapid detection and continuous UV measurements of the EM emission following BNS/NS–BH mergers identified by GW detectors set requirements for rapid spacecraft slew capability, instantaneous access to a large fraction of the sky, real-time communication, and a wide FOV. The early (hour) detection and continuous measurements of UV light curves for hundreds of core-collapse SNe require a high cadence and a large grasp. A wide FOV, with a correspondingly lower

sensitivity for a given grasp, is required in order to obtain a lower characteristic distance, which will enable spectroscopic follow up of a large fraction of detected SNe.

In addition to the study of BNS/NS–BH mergers and SNe, ULTRASAT will provide continuous near-ultraviolet (NUV) light curves for hundreds of tidal disruptions of stars by supermassive black holes (SMBHs), thousands of AGNs, and $>10^5$ flaring and variable stars (See Table 2).

This paper is organized as follows. An overview of ULTRASAT's system design and expected performance is given in Section 2, a description of the currently planned modes of operations of ULTRASAT is given in Section 3, and the Science Operations Center (SOC) is described in Section 4. An overview of the mission science objectives is given in Section 5. A short summary of the expected contributions of ULTRASAT to the key science goals is given in Section 6.

2. Design and Performance

Here we briefly describe the spacecraft, its payload, and performance. ULTRASAT's key performance characteristics are given in Table 1. The ULTRASAT spacecraft will be constructed by the Israeli Aerospace Industry (IAI). It will carry a single instrument—a wide FOV ($\cong$204 deg^2) telescope constructed by Elbit/Elop, with a focal-plane array (FPA; hereafter camera) constructed by Deutsches Elektronen-Synchrotron, including a UV-optimized detector produced by TowerJazz and designed by AnalogValue.

ULTRASAT will be launched to a geostationary transfer orbit (GTO) and then self-perform a GTO–GEO transfer to acquire its final GEO position. It is planned for a minimum 3 yr mission operation, with sufficient propellant for a 6 yr science mission. The mission lifetime is limited by propellant availability for station keeping, and final evacuation from its GEO position to the geostationary graveyard belt.

2.1. Spacecraft

The ULTRASAT spacecraft bus is constructed around two main components: the ULTRASAT wide-field telescope, and the bipropellant propulsion system. The propellant mass contributes about half of ULTRASAT's total launch mass $\sim$ 1100 kg, and is required to enable the GTO–GEO maneuvers. The bus uses high Technology Readiness Levels components and is based on the successful IAI heritage series of small satellites, benefiting from that company's long-term experience in fabricating and operating missions in both low-Earth orbit and GEO. The spacecraft is designed so that it can be attached as a hosted payload inside the launcher.

The spacecraft gimbaled high-gain antennas are designed to support ULTRASAT's data rate ($\sim$5 Mbps), and together with the GEO allow for continuous real-time data download for all allowed pointings (see the pointing restrictions below). In case of a communication failure, images will be stored on the ULTRASAT On-Board Recorder (OBR) and will be downloaded once the communication is restored. The OBR can store images from nearly 8 days of continuous observations with the nominal exposure time (300 s).

In order to enable a quick response to ToOs, ULTRASAT is designed with full-hemispheric telecommand antennas and pointing slew agility ($>0.^\circ5$ s^{-1}), which enable starting observations at any visible position in fewer than 15 minutes from an incoming alert trigger (e.g., of a GW event) at the SOC. ULTRASAT's power system (solar panels and battery) supports at least 3 hr of ToO observations with negative power balance (in survey mode the power balance is always positive, see Section 3.1). Assuming randomly distributed ToOs, a negative power balance will occur for $\lesssim$33% of ToO observations.

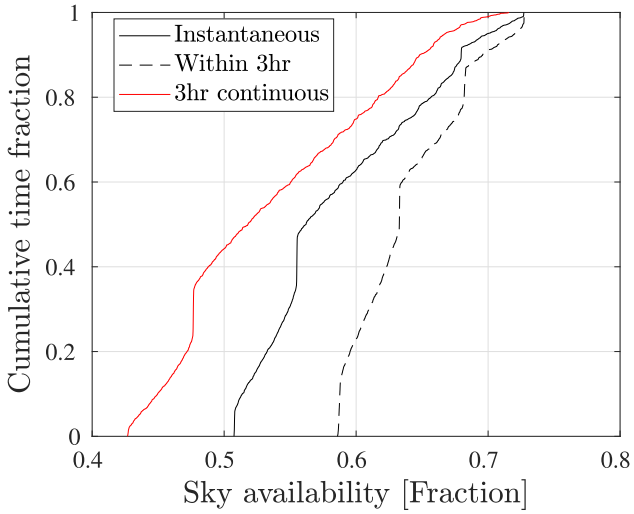

Figure 3. Sky availability for ToO observations under ULTRASAT pointing restrictions. At any given time ULTRASAT can access >50% of the sky, and >58% within 3 hrs. The minimal sky fraction for a 3 hr continuous observation (the nominal ToO duration) is 42%, and the median is 51%.

The (angular sky) directions allowed for ToO observations are limited by stray-light constraints. ULTRASAT is restricted to observe fields for which the optical axis is >70° away from the Sun (this restriction also apply during slewing), >48° from the Earth limb, and >35° from the Moon, in order to limit the stray-light contribution to the background (see Section 2.2 for a discussion of stray-light suppression). Under these restrictions, ULTRASAT can access instantaneously (i.e., at any given moment) >50% of the sky and observe >42% of the sky continuously for at least 3 hr (see Figure 3). The fraction of the sky accessible to ULTRASAT within 3 (6) hours is >58% (>66%).

ULTRASAT's pointing stability ("jitter") of $<3''$ (3σ) over 300 s (the nominal exposure time) is achieved using its attitude and orbit control system (specifically, the star trackers, reaction wheels, and inertial measurement units). For blue sources at radial distance $\sim 5^\circ$ off the FOV center, the jitter contributes significantly to the image point-spread function (PSF), while for blue sources at other locations in the FOV, and for red sources at any location within the FOV, the jitter contribution is negligible (see Section 2.2 and Figure 5 for more details).

2.2. Payload

The ULTRASAT payload has three main components—a baffle, the optical tube assembly (OTA; i.e., the telescope), and the FPA (aka, camera). Below we give a brief overview of each of them. Detailed description of the baffle and the OTA is given in Ben-Ami et al. (2022), and in-depth descriptions of the camera design and characterization are given in Asif et al. (2021) and Bastian-Querner et al. (2021), respectively.

ULTRASAT achieves its wide-field capabilities via a wide-field Schmidt telescope design. A 33 cm diameter double corrector plate, made of a single fused-silica lens and a single CaF2 lens, is mounted at the entrance of the telescope. The 50 cm diameter Zerodur mirror has a clear aperture of 48 cm. A

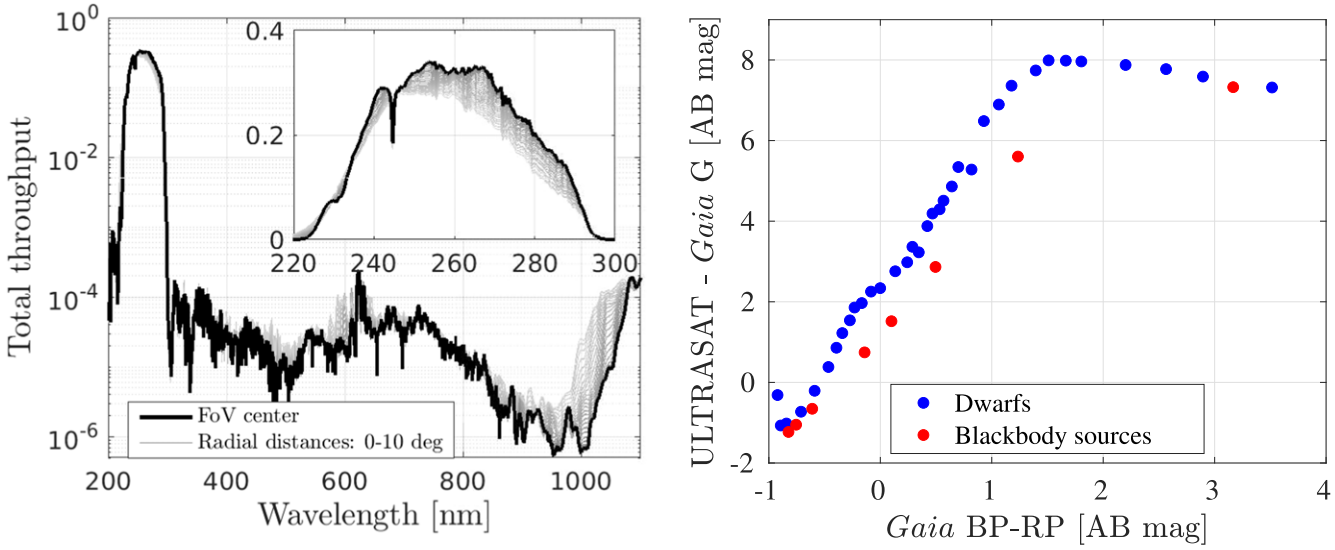

Figure 4. Left: ULTRASAT's total throughput, accounting for all optical elements, the detector's quantum efficiency (QE), and obscuration. The minor variation of the throughput across the FOV (gray curves) is due to the variation of the obscuration and of the AOI distribution. Right: color–color relation between ULTRASAT and Gaia bands, for a range of main-sequence dwarfs (blue dots) and blackbody sources (red dots).

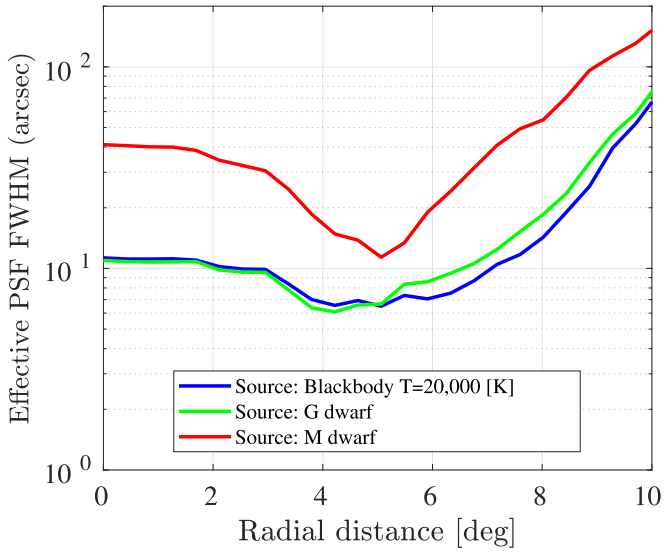

Figure 5. ULTRASAT's radial-dependent effective PSF FWHM for three representative sources—G dwarfs and M dwarfs (dMs), and a $T = 20{,}000$ K blackbody source.

field-flattener assembly, made of a fused-silica lens, a CaF2 lens and a Sapphire filter, is mounted ≈0.55 mm in front of the FPA.

Achieving strong out-of-band attenuation, while maintaining high throughput within the operation band, is crucial for meeting the signal-to-noise ratio (S/N) requirements. The payload design addresses the out-of-band attenuation by minimizing the red leak through a combination of coatings on the sapphire filter, the lenses, the mirror, and the detector. This leads to transmission of only 2.9×10^{-5} (band average) of visible light while maintaining >25% overall in-band throughput. The variation of obscuration and angle-of-incidence (AOI) distribution across the FOV results in a minor radial variation of the overall throughput (see Figure 4).

ULTRASAT's optical design maximizes the system grasp via a chromatic radial-dependent PSF optimized to the ULTRASAT band. Figure 5 gives the PSF FWHM (including spacecraft jitter, thermal variations, and assembly errors) for various sources at different radial positions. The system area-averaged PSF FWHM for a $T = 20{,}000$ K blackbody source in the central 170 deg^2 of FOV is 8.″3.

A 20° slanted baffle is mounted in front of the telescope to prevent stray light from entering the telescope and to reduce Cherenkov radiation. The slanted geometry enables the telescope to point >70° from the Sun without allowing any sunlight into the optical system. The baffle includes vanes to suppress the stray light from the Earth and the Moon, achieving, together with the OTA elements (in particular the sapphire filter and the mirror), better than 2×10^{-11} stray-light suppression.[20] The second main task of the baffle is to suppress the flux of high-energy electrons penetrating the outer corrector lens, reducing by a factor of ≈10 the Cherenkov radiation produced as these electrons propagate through the lens, which is one of the two main noise sources (see Section 2.3).

The FPA consists of four 45×45 mm^2 back-side illuminated CMOS detectors, with 9.5 μm pixels. The camera is shutterless and is read in a rolling-shutter mode, which allows continuous exposures with minimal overhead time (∼2 ms). The entire pixel array is read in less than 20 s. High dynamic range capability is achieved by dual-gain 5T pixels. The high QE in the ULTRASAT wave band is achieved via a high-K dielectric layer and a UV-optimized antireflection coating. See Liran et al. (2022) for more details on the development and characteristics of the ULTRASAT customized sensor.

The FPA is mounted on a spider arm assembly within the telescope tube, thermally isolating the FPA (which operates at 200 K to minimize dark current) from the telescope structure, which is kept at 293 K. The instrumental camera noise (e.g., dark current and read noise) contributes less than 30% to the total background noise variance (see Table 3).

2.3. Sensitivity

ULTRASAT's sensitivity (e.g., limiting magnitude and other S/N calculations) is affected by three types of noise sources—

[20] Stray-light suppression is defined as the ratio between the scattered photon flux produced by a source (e.g., Earth) on the detector and the source photon flux at geostationary orbit.

Table 3
ULTRASAT Estimated Background Noise in a Single 300 s Exposure

Source	Variance (e^- pixel^{-1})
Zodiac (perpendicular to the Sun's direction)	27
Cherenkov (75th percentile high flux)	15
Stray light (max)	12
Dark current	12
Readout noise [squared]	6
Electronic cross talk	2
Gain	1
Quantum yield	<1
Total	75

instrumental, external, and source related. ULTRASAT's design addresses and minimizes each of these, and specifically ensures that for the nominal observations the contribution of the instrumental noises is subdominant. In this section we first describe the contribution of each of the noise sources and then derive the limiting magnitude and S/N for various astrophysical sources. These are used later, in Section 5, to derive their estimated detection rates. The S/N is calculated using publicly available tools (Ofek 2014; MAAT[21]).

For the sensitivity calculations we assume conservative observing conditions (see the details below for each noise source) and a minimal observing visit per pointing of 3×300 s (the three exposures are required to identify reliably and eliminate cosmic-ray signatures). The resulting contributions to the background variance of the various noise sources for a single 300 s exposure are summarized in Table 3. The three external noise sources—zodiacal light, Cherenkov radiation, and stray light—dominate ULTRASAT's background noise. The variation across the FOV of these external noise sources (due to the varying throughput) is negligible (<0.1%).

Zodiacal light. ULTRASAT's out-of-band ($\gtrsim$300 nm) rejection suppresses most of the zodiacal light, mainly by the sapphire filter. The zodiacal light varies with ecliptic latitude and longitude, increasing for observations closer to the Sun with a relatively sharp increase at angles <90° from the Sun. ULTRASAT's survey fields and the all-sky map observations (see Sections 3.1 and 3.3) are planned to always be at $\geqslant$90° away from the Sun. In our reference sensitivity we calculate the zodiacal light for our survey fields close to the ecliptic poles, when they are in a direction perpendicular to the Sun's direction.[22] We use the zodiac spectrum from the Hubble Space Telescope (HST) Space Telescope Imaging Spectrograph (STIS) instrument handbook,[23] and adjust for the ecliptic coordinates using the table from the HST WFC3 instrument handbook[24] The resulting noise of 27 e^- pixel^{-1} per 300 s exposure is the highest background noise.

Cherenkov emission. Trapped energetic electrons hitting the external fused-silica corrector lens are the main source for the Cherenkov radiation illuminating the detector. ULTRASAT's baffle significantly reduces the flux of electrons reaching the outer lens (dominated by the flux entering through the baffle opening angle), and hence the resulting Cherenkov background. The Cherenkov noise contribution was calculated using a detailed Monte Carlo ray-shooting simulation to estimate the energy-dependent electron intensity incident at various depths and radial positions across the outer lens. The electron intensity distribution was then used to derive the resulting Cherenkov emission at relevant angles (for which propagation through the optical system leads to illumination of the detector). The numeric results are consistent with those we obtained using a simplified analytic calculation (confirming in particular that the contribution to the Cherenkov light from optical elements other than the outer lens is negligible). The trapped electron flux at GEO is highly variable on timescales of days, with variations of 3–4 orders of magnitude. For our conservative noise estimations we used the 75th percentile of electron flux based on the AE9 model (Ginet et al. 2013). The resulting Cherenkov noise contribution is about half of the zodiacal contribution. For the 95th percentile electron flux, the Cherenkov noise will be 2.8 times larger, while for the median electron flux it will be 2.5 times smaller (thus already below the instrumental noise). Our estimates of the Cherenkov contribution are consistent with the results of Kruk et al. (2016), who studied the radiation-induced background at GEO and found that for exterior glasses (e.g., an unshielded external lens) zodiacal light dominates at $\gtrsim$300 nm, while Cherenkov radiation dominates at shorter wavelengths (see their Figure 8).

Scattered light. Under our pointing restrictions (described above), scattered light from Earth is the dominant stray-light source. The baffle design (e.g., vanes and Acktar vacuum black coating) was optimized to suppress this contribution. The Earth's flux at GEO was estimated based both on observations made by the Sentinel 5P satellite (Veefkind et al. 2012), and on calculations using solar irradiance and Earth's albedo, with consistent results between the two methods. The stray-light flux reaching the detector was calculated by detailed Monte Carlo simulations of light propagation through the optical system. For our conservative noise estimations we assumed full Earth at the closest allowed angle from the lowest side of the baffle. The resulting stray-light noise contribution is similar to (but slightly smaller than) the Cherenkov noise.

Instrumental noise. ULTRASAT's sensor was designed to minimize instrumental noise (Liran et al. 2022). The nominal sensor design performance was already measured and verified. The sensors are kept at 200 K, yielding a low dark current of <0.05 e^- s^{-1} pixel^{-1}. Long-term radiation effects (i.e., the total ionizing dose) will lead to some increase in the dark current, but the sensors are sufficiently shielded so that the worst-case dark-current increase at the end of the mission is expected to be less than a factor of 2. The read noise was measured to be <2.5 e^- pixel^{-1} (averaged over the PSF, taking into account also the tail of high read noise pixels). The remaining instrumental noise sources—electronic cross talk, gain, and quantum yield—do not contribute significantly to the overall noise.

Resulting sensitivity. ULTRASAT's chromatic and radial-dependent PSF yields a radial- and source-dependent sensitivity. Figure 6 shows ULTRASAT's radial-dependent limiting AB magnitude (5σ detection in three coadded 300 s images) for various point sources, and the S/N achieved with three coadded 300 s images as a function of AB magnitude. For these calculations, we use either the Pickles (1998) spectral flux library for stellar sources or a blackbody spectrum. The measured source flux is derived using ULTRASAT's

[21] https://github.com/EranOfek
[22] We note that ToO observations may be as close as 70° from the Sun, in which case the zodiacal contribution can be up to 35% higher.
[23] STIS instrument handbook, Chapter 6.6, Table 6.4.
[24] WFC3 instrument handbook, Chapter 9.7.1, Table 9.4.

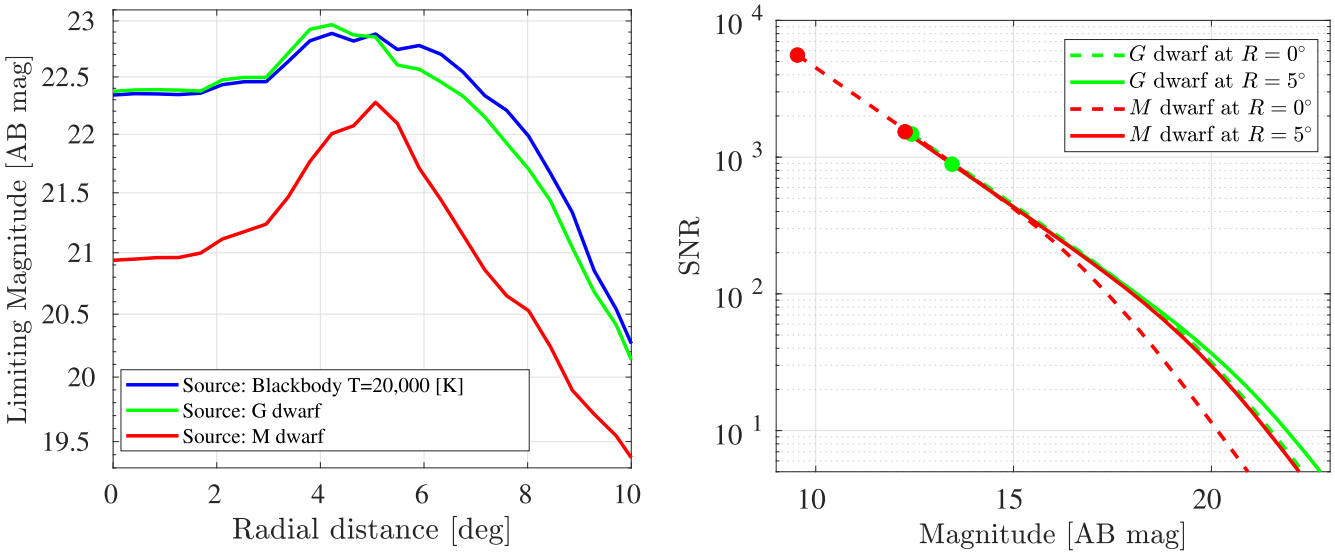

Figure 6. Left: limiting point-source AB magnitude achieved in 3 × 300 s ULTRASAT exposures, plotted as a function of radial distance from the field center. Right: ULTRASAT's S/N as a function of AB magnitude for 3 × 300 s exposures, for G dwarfs and dMs at the FOV center and at $R = 5°$. The dots at the end of each curve mark the saturation limit.

throughput curve and by conservatively assuming 80% PSF photometry efficiency (i.e., 20% source flux losses due to imperfect PSF representation and fitting). The noise is calculated within an effective PSF, which is calculated by applying the ULTRASAT chromatic and radial-dependent PSF to the source spectrum propagated through ULTRASAT's throughput. A faint 24 AB mag host galaxy is assumed for the calculations, thus not dominating the background noise in these estimates.

Confusing limit. ULTRASAT will observe some regions of the sky repeatedly for a total of more than 100–10^4 hr (e.g., the high- and low-cadence survey fields, see Section 3.1). Crowding may become a major issue in deep coadded images of these regions. In Section 5.9, we perform a detailed analysis of the confusion limits as a function of ULTRASAT PSF FWHM, as part of the estimates for the expected galaxy counts. The radial-dependent confusion limit in the central 170 deg^2 of the FOV is in the range 24.0–25.5 AB mag (achieved by coaddition of 200–400 images of 300 s exposures). See Section 5.9 for more details.

3. Modes of Operation

ULTRASAT will have two main modes of operation: (i) survey observations, during which the telescope stares at the same field (or cycle through a few adjacent fields) for a long period, and (ii) ToO observations, a triggered mode where ULTRASAT stops its survey observations and slews to a new position. In addition, at the beginning of the mission an all-sky UV map will be constructed.

During the survey mode, the extragalactic survey volume will be maximized by pointing ULTRASAT at fields near the ecliptic poles, minimizing Galactic extinction, and switching between north and south in summer/winter, minimizing the zodiacal background. Below we describe in some detail our current observing plan, which is used in Section 5 for the calculations related to observations designed for meeting the science goals. This plan will be reevaluated, and potentially revised, before the beginning of the mission and annually during the mission.

3.1. Survey Modes

ULTRASAT will devote ≈90% of its time during the first year to a high-cadence survey, and ≈10% to a low-cadence survey. In both survey modes, the images will be transmitted to the ground in real time. ULTRASAT's SOC will issue alerts of new transients detected by ULTRASAT within 15 minutes from image capture. Every 6 months, as the Sun switches hemispheres, ULTRASAT will slew to the region in the opposite hemisphere. During each semester ULTRASAT rotates about the center of the FOV by ≈1° every ≈1 day to keep the Sun within ≈10° of the solar panels' normal.

High-cadence survey (21.25 hr day^{-1}). ULTRASAT will be pointed toward one predetermined field near the ecliptic poles. The field's selection is based on minimizing both the zodiacal background and Galactic extinction, such that the extragalactic survey volume is maximized. Each field will be observed for 6 months, with continuous 300 s exposures.

Low-cadence survey (2.75 hr day^{-1}). During each seasonal (north/south) dwell ULTRASAT will cycle through 40 fields covering ∼8000 deg^2 (∼6800 deg^2 covered by the central 170 deg^2 of the FOV for which the grasp was optimized), observing 10 fields each day (i.e., a 4 day cadence per field). In this mode, ULTRASAT will stare at a given field for 15 minutes (three consecutive 300 s exposures), and then move to observe a nearby field. The angular distance between adjacent fields will be <40° and the slew time between adjacent fields will be <1.5 minutes. The survey fields will meet the Sun and Moon minimum angle limits during the entire 6 month observing window.

3.2. Target of Opportunity

Upon reception of a ToO trigger command, ULTRASAT will interrupt observations and slew to the designated pointing. At any given moment, >50% of the sky will be available for ToO observations (limited by the pointing restrictions with respect to the Sun, Earth, and Moon). ULTRASAT will slew to any observable point on the sky within <15 minutes from the time a trigger was received at ULTRASAT's SOC. The interruption time per ToO is nominally capped at <3 hr.

ULTRASAT will observe the ToO field continuously with a nominal exposure time of 300 s.

3.3. All-sky UV Map

During the first six months of the mission, ULTRASAT will undertake an all-sky survey of total integration of 6×300 s (1800 s) at low Galactic latitudes ($|b| < 30°$) and 50×300 s (15,000 s) at high Galactic latitude ($|b| > 30°$). The high-latitude survey with an AB limiting magnitude of 23.5–24 mag will be >10 times deeper than the GALEX all-sky survey. Furthermore, it will provide an all-sky UV variability survey.

The all-sky UV map is required as a deep reference image for transient detection using image subtraction; specifically, following triggers of GW events (see more details in Section 5.1). The scheduling of the all-sky map observations will be optimized with respect to the LIGO/VIRGO O5 run.

4. Science Operation Center

The ULTRASAT SOC will be located at the Weizmann Institute of Science in Israel, and will support all scientific aspects of the ULTRASAT mission, including observation planning, data reduction, and alert distribution. The SOC interfaces with the Ground Control Segment (GCS) at IAI, which is responsible for all direct communications with the ULTRASAT spacecraft. The GCS will acquire the spacecraft after separation from the host vehicle and maintain continuous communication through a ground antenna.

The SOC will plan and schedule in advance the survey and all-sky UV imaging observations (see Section 3). In addition, the SOC will receive real-time alerts from several sources (mainly GW events; GRB, TDE, and neutrino triggers are also under consideration). The SOC will send a new immediate ToO observing plan to the GCS in cases where a ToO observation is both relevant (meeting predefined criteria) and feasible (considering, e.g., target visibility and spacecraft power condition). Observations will start within no more than 15 minutes from the time the incoming alert was received at the SOC.

The GCS will distribute the science and telemetry data to the SOC for real-time processing, calibration, and archiving. The ULTRASAT pipeline will generate a large number of data products, the goal of which is to minimize the time required to perform scientific research using the data. Focus is therefore given to quality, diversity, and ease of use. The pipeline is based on the software package described in Ofek (2014) and Ofek et al. (2023b).

4.1. Data Products

The exact structure and content of the ULTRASAT data products are still in development. Here we briefly describe the current plan for these data products, which builds on the LAST pipeline (Ofek et al. 2023b) and the experience gained within that development effort. A detailed description of the procedures and expected data products (e.g., image and source catalog columns) can be found in Ofek et al. (2023b).

All analysis will be done on single-epoch images (i.e., 5 minutes) as well as on coadditions of three images (15 minutes), 30 images (2.5 hr), and ∼250 images (i.e., a daily coaddition of the high-cadence survey data). The data products will include science images (raw, processed, and DIA), auxiliary images (mask, PSF, background, and variance), and source catalogs (extracted from both the reference-subtracted and nonsubtracted science images). Transients will be detected (and if possible classified) from these data products. The images and catalogs will be astrometrically calibrated to Gaia DR3 (Gaia Collaboration et al. 2021; Lindegren et al. 2021), with an expectation to reach an absolute (and relative) position precision of $\lesssim$30 mas at the bright end and $\sim 1''$ for faint sources. Relative photometry for bright sources in the 15 minute coadded images is expected to reach at least ∼1 mmag. Systematic uncertainties are excepted to dominate below that level. Photometric calibration will be based on reference stars for which UV spectroscopy is available through HST and the IUE space telescope. This will be used to assess the overall system throughput in orbit (in addition to the prelaunch assessment). The calibrated photometric measurements will then be provided as AB mag. Absolute photometry is expected to reach ∼10 mmag. Finally, light curves and motion curves will be constructed by cross-matching the catalogs obtained at various epochs. Cross-reference to external archival catalogs (i.e., GALEX) is also planned.

The SOC will issue public alerts of new transients, for both survey and ToO observations, within fewer than 15 minutes of ULTRASAT image acquisition. Each alert will include the transient position, its current flux, and a cross-reference to known sources. All other ULTRASAT data products will be made available on the SOC standard archive via periodic public data releases following full calibration and verification. The proprietary period will be 12 months. Members of the ULTRASAT collaboration will have immediate access to all ULTRASAT data products.

5. Science Objectives

ULTRASAT will detect transient events in an unprecedented large volume of the Universe, and will explore new parameter space in energy (NUV) and timescale (minutes to months). It is thus expected to have a major impact on a wide range of astrophysics topics, with a vast space for serendipitous discoveries. In this section we discuss ULTRASAT's broad scientific impact across the fields of GW sources (Section 5.1), deaths of massive stars (Section 5.2), cosmology (Section 5.3), GRBs (Section 5.4), stars and stellar remnants (Section 5.5), exoplanets and the star–planet connection (Section 5.6), TDEs (Section 5.7), AGNs (Section 5.8), galaxies (Section 5.9), and the solar system (Section 5.10). Table 2 summarizes ULTRASAT's science highlights.

For the detection rate estimates we use the ULTRASAT sensitivity derived in Section 2.3 (see also Figure 6), a FOV of 170 $\deg^2$ (to which the grasp was optimized), and the relevant modes of operation (described in Section 3) for each science case (e.g., survey modes for SNe, ToO for GW alert follow up, and all-sky UV map for asteroid NUV colors). Explicitly for the survey modes, we use an area of 170 $\deg^2$ for the high-cadence survey and a total area of 6800 $\deg^2$ for the low-cadence survey.

5.1. Search for UV Emission from Gravitational-wave Sources

The era of GW astrophysics has begun with the detection of GWs from BH and NS mergers by the laser interferometer observatories LIGO and Virgo (Abbott et al. 2016a, 2017a). The possibilities are many and exciting (Barack et al. 2019; Margutti & Chornock 2021), including new tests of general

relativity, a new probe of stellar death in binary evolution, and determination of the demographics of stellar remnants. Coalescences involving NSs provide unique insights into the physics of our Universe; they are the most likely sites of production of *r*-process elements (e.g., Pt and Au; Fernández & Metzger 2016; Cowan et al. 2021) and provide unique diagnostics of the physics of the densest matter in the Universe (Phinney 2009).

The detection of the associated EM emission will be the key to using these events for addressing fundamental physics and astrophysics questions; it will provide direct constraints on the structure of the ejected material, which will in turn provide unique diagnostics of the properties of matter at nuclear densities and of the merger dynamics; it will enable us to determine whether and which *r*-process elements are produced and whether highly relativistic GRB jets are produced; and it will allow us to localize the mergers precisely. Determining the location in, and properties of, the host galaxy will reveal the stellar antecedents of NS binaries, and the host redshift distribution can be used to measure cosmological parameters, in particular H_0.

By 2027, GW interferometer networks are expected to provide a few to a few tens of detections of mergers involving NSs per year within ≈300 Mpc, with angular localization ~ 100 deg^2 (Abbott et al. 2016b, 2018, 2020). In this era, issues of GW alerts with rough parameter estimates (NS–NS, NS–BH, or BH–BH; rough sky position; and distance) are expected within minutes and with refined parameters within hours.

With a large fraction (>50%) of the sky instantaneously accessible, fast (minutes) slewing capability, and a FOV that covers the error ellipses expected from GW detectors beyond 2026, ULTRASAT will rapidly detect and provide continuous UV light curves of the EM emission following BNS mergers identified by GW detectors. The alerts provided by ULTRASAT will further enable early ground- and space-based follow-up spectroscopy and monitoring at other wavelengths.

In Section 5.1.1 we show that the distance out to which the EM emission will be detectable by ULTRASAT is expected to exceed the ≈300 Mpc horizon of the GW detectors. In Section 5.1.2 we discuss ULTRASAT's advantages, compared to the capabilities of other surveys, in detecting EM emission following GW events. In Section 5.1.3 we discuss the unique constraints that will be provided by early (hour timescale) light curves, in particular in the UV, on the structure and composition of the merger ejecta.

5.1.1. Detecting UV Emission following Binary Neutron Star Mergers

Direct calculations of the structure and composition of the ejecta produced in NS–NS/BH mergers are highly complicated and computationally demanding since they involve a density range of over 30 decades, the entire periodic table, subrelativistic to relativistic flows, and require consideration of neutrino transport, general relativity, and magnetic field effects (Shibata & Hotokezaka 2019; Radice et al. 2020; Rosswog & Korobkin 2022). Modeling the EM output is thus a challenging but vibrant field (Fernández & Metzger 2016; Nakar 2020; Margutti & Chornock 2021).

Many models predict a UV signal with a 10^{41}–10^{42} erg s^{-1} luminosity lasting for hours to a day, which may be produced by different ejecta components (see Fernández & Metzger 2016; Nakar 2020; Margutti & Chornock 2021 for reviews; and recent analyses by Banerjee et al. 2020; Dean et al. 2021; Banerjee et al. 2022; Combi & Siegel 2022; Hamidani & Ioka 2022): free neutron beta decay in high-velocity matter, high-Y_e ejecta with lower *r*-process element content and opacity, hot low-Y_e ejecta, and boosted relativistic material and/or shock cooling. These predicted signals will be detectable by ULTRASAT out to ≈300 Mpc.

The detection of EM emission following the nearby (40 Mpc) NS merger event GW170817 lends strong support to the estimates of the expected UV signal, and highlights the advantages of ULTRASAT as an EM counterpart detection machine. The EM counterpart of GW170817 (AT 2017gfo) was detected 10 hr following the merger, with a luminosity of 10^{42} erg s^{-1} and a temperature exceeding 10,000 K. The absolute NUV magnitude of AT 2017gfo was about −14.5 at about 0.6 day after the merger. Furthermore, the NUV light curve was possibly decaying between the two first epochs, indicating that the NUV peak luminosity was earlier and brighter. Given these parameters, ULTRASAT can detect AT 2017gfo–like events to a distance of about 240 (400) Mpc, in 15 minutes (2 hr) integrations. However, it is likely that the AT 2017gfo was brighter in NUV in earlier times. In this case, ULTRASAT may detect these events to larger distances.

5.1.2. ULTRASAT's Advantages in Detecting Electromagnetic Emission following GW Events

Major ground-based optical/IR (OIR) facilities will also react to GW events. These facilities have the sensitivity to detect the optical emission, but have much lower real-time sky accessibility (∼6% per location, given day/night, horizon, moon, and weather effects).

The ground-based detection of EM emission 10 hr following GW170817, by targeting known galaxies in the GW source error volume, is an impressive result. However, earlier detection would be crucial for obtaining spectra and early light curves, which are essential for determining the properties of the ejecta (see more below). Furthermore, although the GW angular localization is expected to improve to 10–100 deg^2 by 2027, EM transient identification will remain challenging as the GW detection horizon is increased to ≈300 Mpc, implying a larger error volume containing hundreds to thousands of galaxies and fainter signals with a larger number of background transients that would need to be classified.

Before the launch of ULTRASAT, several more GW events with exceptional properties (dense interstellar medium or a rare on-axis orientation) might have been localized to their host galaxies. If so, the EM/GW frontier will be in early localization, constructing larger, unbiased samples, and performing detailed studies of BNS mergers, for which ULTRASAT is ideally suited.

Finally, let us comment about EM searches in other bands. It is generally accepted that GW events involving NS can produce short hard GRBs. So X-ray and gamma-ray searches are clearly useful. However, there is sound empirical evidence that the prompt high-energy emission is strongly "beamed" (conical emission). Only ∼1 in 100 events will be aimed toward us and detectable at high energies, to distances larger than tens of megaparsecs. This is well supported by the very weak X-ray and gamma-ray counterparts of GW170817, which would not have been detectable beyond 60 Mpc. The explosive energy of the coalescence will also drive a strong shock in the ambient medium, from which radio emission is expected to be detectable after months to years. The radio channel is attractive

because it is isotropic. However, the long delay precludes key observational diagnostics for *r*-process elements—specifically OIR spectroscopy on timescales of days to a week. This conclusion is also well supported by the radio emission from GW170817, which was detected with a 2 week time delay despite its proximity.

5.1.3. The Importance of Early UV Measurements

Despite the extensive observations and study of the EM emission following the nearby BNS merger GW170817, large uncertainties remain regarding both the structure and the composition of the ejecta.

[1] The observed UV-IR emission is consistent with the emission of radiation from a mildly relativistic expanding ejecta, which is being continuously heated by radioactive energy release at a rate corresponding to radioactive elements heavier than the iron group (e.g., Cowperthwaite et al. 2017; Drout et al. 2017; Kasen et al. 2017; Perego et al. 2017; Tanaka et al. 2017; Rosswog et al. 2018; Waxman et al. 2018). This is remarkably consistent with the kilonova (KN) emission predicted to follow NS mergers Fernández & Metzger (2016). However, the detailed properties of the ejecta, which are inferred from observations, are inconsistent with those obtained in merger simulations (see Nedora et al. 2021 for a recent and detailed discussion). In particular, the mass of the ejecta is larger than obtained in simulations, and it is difficult to explain (e.g., Fujibayashi et al. 2018; Metzger et al. 2018; Waxman et al. 2018) the existence of a fairly massive, $\simeq 0.05\,M_{\odot}$, fast, $v \sim 0.3c$, component with low opacity corresponding to a large initial electron fraction Y_e and a low lanthanide mass fraction $X_{\rm Ln}$, which is inferred from the early UV/blue emission (Waxman et al. 2018). Alternative models have thus been proposed, in which the blue emission is produced by boosted relativistic material and/or shock cooling of an expanding mildly relativistic shell (e.g., Kasliwal et al. 2017; Gottlieb et al. 2018; Piro & Kollmeier 2018). In some of these cases, the UV emission may depend on the viewing angle, and can help in distinguishing between different models.

[2] The abundances of elements produced in GW170817 are not yet clear. The blue to red evolution of the emission may be explained by the existence of several ejecta components characterized by largely differing compositions, with higher-opacity components corresponding to $X_{\rm Ln} \approx 10^{-1.5}$ dominating at later times (Cowperthwaite et al. 2017; Drout et al. 2017; Kasen et al. 2017; Perego et al. 2017; Tanaka et al. 2017; Rosswog et al. 2018). We have shown (Waxman et al. 2018; see also Smartt et al. 2017) that an alternative explanation is possible, in which the entire ejecta are composed of low-opacity material corresponding to $X_{\rm Ln} \approx 10^{-3}$, spanning a wider velocity distribution than previously assumed. Inferences of composition based on spectral analyses (e.g., Watson et al. 2019; Hotokezaka et al. 2021; Domoto et al. 2022; Gillanders et al. 2022; Hotokezaka et al. 2022; Perego et al. 2022; Pognan et al. 2022) are challenged by the partial atomic data (opacities and excitation/ionization cross sections) available for heavy elements, and by the large density of lines of such elements combined with relativistic expansion velocities. Watson et al. (2019), Gillanders et al. (2022), and Perego et al. (2022) find that features in the early ($\sim$1 day) spectra may be explained as due to first-peak *r*-process elements (Sr and Zr) with low $X_{\rm Ln}$ ($<5 \times 10^{-3}$; Gillanders et al. 2022), while $X_{\rm Ln}$ values inferred from (i.e., the large IR opacity implied by) later spectra differ widely between different analyses (Waxman et al. 2018; Domoto et al. 2022; Gillanders et al. 2022).

Different models for the structure and composition of the ejecta differ in their predictions for the early, hour timescale emission, in particular in the UV. Earlier detection of the EM transients and early UV light curves will therefore be highly useful for discriminating between these models (e.g., Arcavi 2018; Banerjee et al. 2020; Dean et al. 2021; Banerjee et al. 2022; Combi & Siegel 2022; Dorsman et al. 2022; Hamidani & Ioka 2022; Werner et al. 2022).

5.2. Characterizing the Death of Massive Stars

Most stars with masses $> 8\ M_{\odot}$ end their lives in SN explosions, which create and distribute the majority of the heavy elements (e.g., Woosley et al. 2002). The explosion mechanisms are a subject of vigorous research. Theoretical models begin with initial conditions—the assumed structure of a model star—and attempt to predict the properties of the resulting explosion. Progress thus requires assembly of a data set connecting observations of preexplosion stars with measured explosion properties. Such observational constraints are critical, but exceedingly scarce—few SNe have an identified progenitor visible in preexplosion imaging (e.g., Smartt 2015), and few more are likely to be found in the foreseeable future, due to the low rate of such events in very nearby galaxies where individual stars can be observed. Charting the fate of the diverse populations of massive stars to specific explosive outcomes is important in order to elucidate the feedback of massive stars on their gaseous environments, and their role in galaxy evolution.

Detection of SNe shortly after explosion and observations following the early emission from such events will enable dramatic advances in our understanding of the way massive stars evolve shortly prior to explosion, the connection between the properties of the progenitor stars and the resulting explosions, and the physics of the explosive process.

The earliest emission of radiation from a SN explosion is associated with "shock breakout" (e.g., Waxman & Katz 2017; Levinson & Nakar 2020). As the radiation-mediated shock that drives the ejection of the SN envelope expands outwards, the optical depth of the material lying ahead of it decreases. When the optical depth drops to $\sim c/v_{\rm shock}$ where $v_{\rm shock}$ is the shock velocity, radiation escapes and the shock dissolves. Such breakout may take place once the shock reaches the edge of the star, producing a bright, 10^{44}–10^{45} erg s^{-1}, X-ray/UV flash lasting typically over the progenitor light-crossing time R_*/c (seconds to a fraction of an hour, depending on the radius of the exploding star R_*), forming the first EM signal that can reach an external observer.

Alternatively, the breakout may take place at larger radii, within the circumstellar material (CSM) ejected from the progenitor star prior to the SN explosion, e.g., by a steady stellar "wind" or by an episodic ejection of an outer envelope shell, provided that the CSM optical depth is larger than $c/v_{\rm shock}$ (e.g., Ofek et al. 2010). In this case, the breakout timescale may be extended from of order hours to many days (e.g., Ofek et al. 2010).

Following the shock breakout flare, the hot ejecta cool and expand, emitting UV/optical emission from the expanding envelope (the "shock-cooling" phase), with $L \sim 10^{43}$ erg s^{-1} on a day timescale.

5.2.1. Simple Shock Breakout Observations

Due to the short duration of the breakout pulse, only a handful of cases have been observed with an indication for a breakout signal (e.g., Campana et al. 2006; Gezari et al. 2008b, 2015; Schawinski et al. 2008; Soderberg et al. 2008). ULTRASAT will change that.

For spherical stars with standard density profiles, and lacking a dense CSM, the duration of the shock breakout flare provides a direct measurement of the stellar radius at explosion (R_*/c). This duration ranges from minutes to about an hour for supergiant stars, making the ULTRASAT cadence uniquely powerful to obtain such measurements.

However, the observed duration may be dominated by the intrinsic pulse duration rather than by the light travel time, R_*/c, as well as by differences in the arrival time of the shock to the stellar surface at different (angular) positions in strongly aspherical explosions or progenitors (Katz et al. 2012; Afsariardchi & Matzner 2018). In such cases, the breakout flare temporal structure provides instead a unique probe of the preexplosion inner structure of the progenitor star, which is mostly inaccessible to other probes.[25]

Though theoretical details of the shock breakout flares at very early times (<1 hr) are still debated (see, e.g., Figure 1 of Ganot et al. 2016), the UV shock breakout emission must match smoothly to the well-understood and observed subsequent shock-cooling phase. The high temperature of the breakout and shock cooling implies that the UV and optical bands are in the Rayleigh–Jeans regime. The decrease in flux due to falling temperature is nearly offset by radial expansion. Thus, for large (supergiant) progenitors the ratio of breakout to shock-cooling flux is close to unity at a few hours. Using these robust flux estimates and observationally calibrated event rates we can determine that ULTRASAT is expected to detect about 15 flares per year (Ganot et al. 2016; see Figure 2).

5.2.2. Circumstellar Medium Shock Breakout Observations

Consideration of CSM breakouts is motivated by, e.g., the indication that pre-SN "precursors" are common for Type IIn supernovae (SNe IIn; e.g., Ofek et al. 2014b; Strotjohann et al. 2021) and occur also in other SN types (Foley et al. 2007; Jacobson-Galán et al. 2022). These month-long precursor events occurring within the final years prior to explosion provide direct evidence for intense mass-loss episodes in many SN progenitors shortly before the explosion. This challenges the canonical picture (e.g., Langer 2012) of a rapidly evolving (through nuclear burning) core surrounded by a nearly time-independent envelope. Various mechanisms have been proposed to generate rapid mass loss, including pair instability pulsations (Woosley et al. 2007), convection- and radiation-driven instabilities (Suárez-Madrigal et al. 2013; Smith & Arnett 2014), waves excited by core convection (Quataert & Shiode 2012; Fuller & Ro 2018), and common envelope interaction (Chevalier 2012; Soker & Kashi 2013).

Observations of CSM breakout flares provide information about the properties of the surrounding CSM, and, most interestingly, on the rate and duration of the mass-loss episode (e.g., Ofek et al. 2010), which map the violent preexplosion evolution of massive SN progenitors, which is observationally hard to observe and theoretically poorly understood.

The recent nearby SN 2023ixf in M101 provides an excellent example for such a case, and several papers have analyzed this object in the context of a CSM breakout (e.g., Hiramatsu et al. 2023; Jacobson-Galán et al. 2023). Zimmerman et al. (2023) show in detail the impact of UV observations, similar to those routinely expected from ULTRASAT, for such analysis, and are able to recover a complete mapping of the CSM structure around the progenitor of this event.

Furthermore, nonrelativistic CSM breakouts are interesting because they may be the sources of several classes of powerful transients. Nonrelativistic CSM breakouts are considered as possible explanations of (at least part of) the SLSN class (Ofek et al. 2010; Balberg & Loeb 2011; Chevalier & Irwin 2011; Ginzburg & Balberg 2012; Moriya et al. 2013), of "double-peak" SNe, of some rapidly evolving transients (e.g., Margalit 2022), and of the early part of the emission of SNe IIn (Ofek et al. 2014a). Specifically, early UV observations were found to be essential to estimate accurately the temperature, radius, and bolometric luminosity of interacting SNe, because they provide a better handle on the blackbody spectrum shape compared to visible light alone. Such observations have recently shown that SNe IIn are hotter and brighter than previously thought, with their radius growing faster (Soumagnac et al. 2020b). Additionally, early UV observations can help determine the geometrical distribution of the CSM surrounding these events, shedding light on the mass-loss processes which occur before the explosion and on the nature of the progenitors. Recent studies using early UV observations have found that at least a third of SNe IIn have a nonspherical CSM (Soumagnac et al. 2019, 2020b), challenging the usual assumption of spherically symmetric models. ULTRASAT will provide UV light curves for about 1000 SNe IIn and will enable such studies on a much larger scale. This could open a new chapter in the study of SNe IIn, allowing for a stronger constraint on the number of aspherical CSM cocoons and bringing us closer to understanding their progenitors and explosion physics.

Relativistic breakouts are also very interesting, especially for high-energy signals (e.g., GRBs and X-ray flashes; Tan et al. 2001; Calzavara & Matzner 2004; Campana et al. 2006; Waxman et al. 2007; Budnik et al. 2010; Katz et al. 2010; Nakar & Sari 2012). ULTRASAT detection and prompt alerts of such rare phenomena could provide highly interesting information.

5.2.3. Shock Cooling Observations

Following the breakout flare, the shock-cooling emission phase provides additional unique signatures of the structure of the progenitor star (including radius, envelope mass, and surface composition) and of its mass-loss history close to the explosion (and possibly also of CSM density inhomogeneities; e.g., Fryer et al. 2020; Goldberg et al. 2022).

For nonrelativistic ($v/c < 0.1$) breakouts from stellar surfaces, existing theoretical analyses (e.g., Nakar & Sari 2010; Rabinak & Waxman 2011; Katz et al. 2012; Sapir et al. 2013; Sapir & Waxman 2017; Kozyreva et al. 2020; Piro et al. 2021; Morag et al. 2022) provide a good understanding and tools for accurate description of the radiation emitted during and

[25] We note though that the $>R_*/c$ breakout duration, obtained in the 3D calculation of a breakout from a convective RSG envelope in (Goldberg et al. 2022), is dominated by the intrinsic duration of the pulse (which is significantly longer than R_*/c for the chosen progenitor parameters), rather than by the convective density inhomogeneities (Morag et al. 2022).

following breakout (see Waxman & Katz 2017; Levinson & Nakar 2020, for reviews).

Early SN observations were used to set, utilizing these theoretical analyses, important constraints on the progenitors of SNe of Types Ia, Ib/c, and II (Maoz et al. 2014; Waxman & Katz 2017; Andrews et al. 2019; Soumagnac et al. 2020a; Levinson & Nakar 2020; Irani et al. 2023, 2024; Pearson et al. 2023). A major challenge facing utilizing the early emission for a systematic study of SN progenitors and explosion parameters is obtaining the required early, <1 day, high-cadence, ~1 hr, multiband observations; for most shock-cooling observations, early multiband observations, including in particular at short, UV, wavelengths, are not available at the high cadence and accuracy required for an accurate determination of model parameters (see, e.g., Rubin et al. 2016; Soumagnac et al. 2020a; Ganot et al. 2022, for examples and discussion). UV measurements are essential for an accurate determination of the high color temperature (Rabinak & Waxman 2011; Rubin et al. 2016; Sapir & Waxman 2017); high-cadence multiband observations are required for a determination of the relative extinction (Rabinak & Waxman 2011), which strongly affects the inferred luminosity and color temperature. ULTRASAT will revolutionize this field, with both the quantity and quality of data expected to improve significantly. This will enable a systematic and accurate determination of progenitor and explosion parameters based on shock-cooling, and possibly shock breakout, observations.

In summary, studying the early SN emission provides unique information on the SN progenitor and its preexplosion evolution, which cannot be directly inferred from later-time observations. This information is highly instructive for studies of the SN explosion mechanisms, which are not fully understood despite many years of research (e.g., Maoz et al. 2014; Janka et al. 2016; Burrows & Vartanyan 2021).

5.3. Cosmology and Type Ia Supernovae

Standard candles such as Type Ia supernovae (SNe Ia), plateau Type II core-collapse supernovae (SNe IIP), and KNe can be used to derive distances in the Universe. Together with redshifts these constrain the physical properties of the Universe at large scales. Distant SNe Ia were fundamental in the discovery of the accelerated expansion of the Universe and the existence of dark energy (Riess et al. 1998; Perlmutter et al. 1999). More recently, standard candles in our local neighborhood indicate that the local expansion velocity (Hubble constant) is in tension with values predicted based on cosmic microwave background observations (Riess et al. 2019; Wong et al. 2020; however, see Rigault et al. 2015; Mortsell et al. 2022). Looking toward the future, large FOV surveys such as ZTF and LSST will provide tens of thousands of SNe at intermediate distances (The LSST Dark Energy Science Collaboration et al. 2018; Feindt et al. 2019). These samples can be used to construct peculiar velocity maps of the full distribution of matter, i.e., also including the otherwise "invisible" dark matter (Kim et al. 2019a). Standard candles, observed at different redshifts, thus uniquely allow us to probe all aspects of cosmology, from the nature of dark energy and dark matter through tests of the early Universe to tests of general relativity. Today, the discovery and classification of large numbers of transients have been largely streamlined (Nordin et al. 2019; Fremling et al. 2020) and the fundamental limitation has instead shifted to the possible impact of systematic effects (Brout et al. 2019). Even rare objects, such as KNe and strongly lensed SNe, where any discovery provides immediately new insights (Abbott et al. 2017b; Goobar et al. 2017), are facing systematic uncertainties. In the following, we discuss how ULTRASAT observations can have significant impact on these cosmology related questions.

5.3.1. Type Ia Supernovae: Progenitors, Dust, and Cosmology

Thousands of SNe Ia have been observed with high precision during the last decade, but these observations, typically occurring around peak light, have still not answered the fundamental question of what triggers the explosion. A SN Ia is driven by the thermonuclear explosion of a WD, but the exact nature of the precursor system and how the explosion is ignited is still not known. Two main progenitor scenarios have been identified, either involving the merger of two DD WDs or mass transfer from a companion onto a SD WD (Maeda & Terada 2016; Livio & Mazzali 2018). For each of these, further unknowns create additional uncertainty: is the companion a main-sequence, giant, or helium star, and what is the role of the CSM (SD)? How violent and clumpy is the merger, and is the detonation caused by an initial explosion in an outer layer of material (DD)? It is likely that several of these explosion scenarios are realized in nature, which could map to the intrinsic diversity among SNe Ia (Pakmor et al. 2013; Soker 2019). The question about the progenitors, besides being of fundamental interest, also implies a systematic uncertainty for cosmology as the potential progenitor scenarios can be expected to evolve differently with time or occur more frequently in some galactic environments. As an example, DD scenarios involving two degenerate objects can be expected to be found also long after star formation occurred while SD models typically require younger companion stars (Maoz & Mannucci 2012). Observational evidence does suggest that cosmological differences between SNe Ia in different environments exist (Rigault et al. 2013). Any unaccounted difference in luminosity between these progenitor classes could quickly bias cosmological constraints.

Light curves of SNe Ia are famously standard close to peak light, as the strength of the detonation erases the signatures of the progenitor setup. Distinguishing these instead requires one to observe at very early phases (or very late). Comparisons between theoretical predictions yield significant differences during the first hours/days (Piro & Morozova 2016; Noebauer et al. 2017; Magee & Maguire 2020). This is particularly true for the SD scenario, where the expanding ejecta is expected to interact strongly with the companion star for certain viewing angles (Kasen 2010; Boehner et al. 2017).

Extensive searches during the last decade have yielded claims of individual SNe both with and without an early flux excess (e.g., Nugent et al. 2011; Cao et al. 2015; Kromer et al. 2016; Hosseinzadeh et al. 2017; Jiang et al. 2017; Miller et al. 2018, 2020; Siebert et al. 2020; Dimitriadis et al. 2023; Lim et al. 2023), but consistent studies of larger samples are limited and hard to interpret (Bianco et al. 2011; Milne et al. 2013; Olling et al. 2015; Nordin et al. 2018; Fausnaugh et al. 2021; Burke et al. 2022). In particular, it has been seen that both the SD and DD scenarios are expected to produce early variability through effects such as Ni mixing or heating from outer Ni shells/clumps (Magee et al. 2021).

UV observations have the power to solve the progenitor puzzle finally, as the additional information allows one to

disentangle the currently discussed models: companion interaction is expected to produce a shock-like signature at early times where the flux increase is even larger at short wavelengths, while radioactive material distributed to the outer ejecta will at least partially absorb UV emission (Maeda et al. 2018). As it is now likely that multiple explosion channels exist, and that each could be associated with stochastic variations (e.g., due to viewing angle), a significant statistical sample of $O(100)$ SNe Ia with early (<3 days) UV observations will be needed. ULTRASAT is uniquely positioned for obtaining this sample, and thus for solving the long-lasting progenitor debate.

An ULTRASAT SN Ia sample could also be used directly to improve SN Ia distances and thus cosmological parameter estimates. The standardized SN peak magnitude for large samples currently displays an intrinsic scatter of around 0.13 mag (Betoule et al. 2014), but several extended standardization methods shows that the underlying true intrinsic dispersion is likely at least 30% lower (Fakhouri et al. 2015). *U*-band features have been shown to be one possible way to achieve this reduction (Nordin et al. 2018). An improved intrinsic dispersion directly translates into improved cosmological constraints, in a way which for example an increased sample does not. Interestingly, a low-redshift SN Ia sample observed in the ULTRASAT band (in addition to the optical bands accessible with many surveys) maps well to the *g* band of the LSST survey for SNe Ia detected at redshifts $z \sim 0.9 \pm 0.1$, allowing for a sensitive test for SN Ia evolution over more than half of the Universe's age. So far, only a handful of SNe Ia have good UV coverage, but already this small sample shows interesting signs of variation not easily captured in standard light-curve analysis (Brown et al. 2018). It is plausible but untested that the standardization potential extends, or even increases, into the UV. If this would be the case, ULTRASAT observations could be used immediately to improve cosmological constraints.

Photon absorption and/or scatter by dust along the line of sight constitutes a fundamental uncertainty for luminosity distances to both SNe Ia and SNe IIP (Goobar & Leibundgut 2011). This effect causes a systematic bias whereby objects appear fainter, and thus more distant, than they really are. Extinction is routinely corrected for as dust absorption is stronger at bluer wavelengths, assuming color measurements are obtained (Cardelli et al. 1989; Schlegel et al. 1998). However, for cosmology this corrections needs to be accurate at the 1% level, far below what standard methods provide (Berger et al. 2003). Reaching this level requires knowing both the intrinsic transient color as well as the wavelength dependence of the dust absorption. The distribution and property variations of dust is only well studied in the most nearby galaxies, while SNe are more likely to explode in particular (star-forming) galactic environments. An extreme example of this is the potential existence of dust in the immediate SN environment, possibly previously ejected, which might evolve in time through the interaction with the explosion itself.

In fact, attempts to model reddening of SNe Ia empirically during recent decades have yielded models that vary significantly from the expected properties of any kind of dust (Schulze et al. 2014; Amanullah et al. 2015). The potential cause of this difference was at the core of the different approaches taken by the two teams who detected the expansion acceleration, and it has not yet been resolved. The underlying problem is that SNe are typically observed at optical wavelengths where it has turned out to be difficult to separate variations due to dust absorption with intrinsic variations in the SN spectral energy distribution (SED). Both can reasonably be expected to vary, e.g., with the surrounding environment.

The ULTRASAT observations have the opportunity to reform fully our understanding of dust absorption of SNe through directly probing the kind of dust individual SNe have encountered, as well as look for any variation in time. This is because different dust models show significant variations in the UV, even for similar amounts of extinction in the optical. In addition, extinction in the UV is very pronounced, making this an easy observation. So far, such studies are confined to only a small set of SNe Ia observed in the UV by HST (Amanullah et al. 2015).

5.3.2. Type Ia Supernovae: Rates

Estimating the expected rate of SNe Ia observable by ULTRASAT is difficult, since the established emission parameterizations do not extend into the UV (e.g., Guy et al. 2007; Kenworthy et al. 2021), and theoretical models show a large variation. Nevertheless, in order to obtain a robust estimate of the expected rate, we have used the fact that the rest-frame UV band of high-redshift SNe Ia falls into the well-observed optical bands. We focused on data from the SNLS (Betoule et al. 2014). The redshifted *g*-band light curves from SNLS can be approximated as rest-frame ULTRASAT UV light curves for a redshift $z = \lambda_g/\lambda_{\rm UV} - 1 \approx 0.92$, where $\lambda_g \approx 5000$ Å and $\lambda_{\rm UV} = 2600$ Å. The difference in limiting magnitudes between the SNLS *g* band and ULTRASAT translates to a redshift ~ 0.2, up to which ULTRASAT would still have similar sensitivity. The SNe Ia of the SNLS/Joint Light Curve Analysis sample within the range $z = 0.92 \pm 0.1$ were analyzed for emission in the SNLS *g* band. The light curves of the 46 objects in the high-redshift bin were evaluated both by eye, and by using statistical information. 17 objects where selected that have at least one UV detection, i.e., 37% of the initial sample. Given the high redshifts of the SN Ia sample, we must expect a significant Malmquist bias. Indeed, in comparison to a large sample of local SNe Ia from ZTF, it became evident that the SNLS SNe Ia are missing redder objects ($c < 0.1$). The redder objects make up about 50% of the ZTF sample, and accordingly, and it is unknown if these would show UV emission if probed with a more sensitive instrument (if the reddening is due to dust one would expect to observe a large fraction of the nearby objects). Accordingly, a conservative assumption is that the 50% missing red objects are not detectable in the UV.

Combined, we can make a robust prediction that $\geqslant$18% of SNe Ia below a redshift of 0.2 are detectable in the UV by ULTRASAT. For a volumetric rate of SNe Ia of $3 \times 10^{-5}\,{\rm Mpc}^{-3}\,{\rm yr}^{-1}$ (Dilday et al. 2010) and the low-cadence survey area, the rate will be $\geqslant$250 (2000) SNe Ia per year up to a redshift of 0.1 (0.2). This are sufficient statistics to make the above mentioned studies promising.

5.3.3. Hubble Constant from Kilonovae, Time Delay of Lensed Supernovae, and other Exotic Transients

GWs can function as cosmological sirens and in principle allow subpercent measurements of the Hubble parameter, H_0

(Schutz 1986; Abbott et al. 2017c). The major uncertainties are caused by the distance measurement and inclination of the GW source, both almost fully degenerate with H_0. The redshift can most easily be determined from the detection of the optical counterpart (KN) caused by a NS merger. The most promising methods for estimating inclination focus either on measuring the GRB afterglow time delay, the color evolution of the early KN light curve, or through polarimetry (Bulla et al. 2022). Both the afterglow as well as the early KN evolution are prime targets for high-cadence ULTRASAT observations. Current radiative transfer KN studies do not focus on the UV region, but it is clear that the dominant inclination effect is in the u band (the bluest band included), where inclination causes a 4 mag variability during the first day after explosion (Bulla 2023). The opacity difference between the "blue" and "red" KN components is likely even stronger at UV wavelengths, making colors based on ULTRASAT observations an excellent inclination indicator.

An alternative path to measure the Hubble constant is the time delay between multiply (strongly) lensed transient sources. This technique has now reached maturity for lensed quasars (Wong et al. 2020) and is expected to become of use for SNe within the next years (Goldstein et al. 2018). As gravitational lensing is achromatic, ULTRASAT will not in itself increase the sensitivity for strongly lensed sources. However, as the cosmological constraint directly depends on the precision with which the time delay can be measured, blue and short-lived events such as the shock breakout of core-collapse SNe could allow ULTRASAT to measure the time delay between strongly lensed events even when these cannot be spatially resolved. Such events are rare, but the shorter signature will allow one to probe less massive lenses, which can increase the rate compared to that of current surveys. A sample characteristic signature would be a shock breakout with multiple peaks which evolves into an overluminous SN (during which the time difference cannot be seen).

5.4. Gamma-Ray Bursts

ULTRASAT will enable GRB studies both through ToO follow up and through direct detection of their UV counterparts in time-domain fields.

While GRB afterglows are effectively panchromatic, and NUV observations probe roughly the same phenomena as optical observations, ULTRASAT has significant strengths for GRB astrophysics. First, its combination of sensitivity, FOV, duty cycle, and response time stands out among present and near-future facilities. Second, the NUV sky has a lower density of confounding sources (both steady and transient) than the optical sky. Third, because NUV observations are more sensitive to dust extinction than optical or near-infrared (NIR) observations, ULTRASAT data may effectively probe dust columns along GRB sight lines.

Approximately 10 cosmological GRBs per year are expected to occur within ULTRASAT's FOV. UV afterglow emission from these GRBs can be detected to cosmological distances, given ULTRASAT's sensitivity. Moreover, prompt emission may also be detected, provided the fluence within a 300 s ULTRASAT exposure exceeds the detection limit. A typical prompt UV luminosity of $>10^{45}$ erg s^{-1} and a prompt emission duration ~ 10 s is sufficient up to a luminosity distance $d_L \approx 5$ Gpc, corresponding to redshift $z \sim 0.8$.

ULTRASAT may be particularly valuable in constraining the existence of orphan GRB afterglows and of dirty fireballs.

GRBs may be part of a larger class of cosmological fireballs. Such fireballs are generically expected when a sufficiently large amount of energy is released into a sufficiently small volume along with a (relatively small) quantity of ordinary baryonic matter. This results in optically thick conditions, so that a large part of the energy is converted into kinetic energy of ejecta. The smaller the baryon loading is, the more relativistic the ejecta become. For bulk Lorentz factors $\Gamma \gtrsim 100$, internal shocks within the ejecta and/or external shocks between ejecta and ambient medium can produce gamma rays. However, there is no a priori reason that "dirty fireballs," which are physically similar apart from larger baryon loading and lower peak Lorentz factors, could not exist. Such explosions would not produce much gamma-ray emission, but could resemble GRBs in most other ways. In particular, they could still produce bright transients with properties similar to GRB afterglows at longer wavelengths, including the NUV.

Afterglows without accompanying gamma rays may also be expected as a consequence of GRB collimation. Relativistic beaming of photons has a characteristic half-angle $\sim 1/\Gamma$. When ejecta from a fireball that are collimated into angle $\theta_{\rm jet}$ decelerate to $\Gamma < 1/\theta_{\rm jet}$, the fireball becomes visible at viewing angles $\theta_{\rm obs} \sim 1/\Gamma > \theta_{\rm jet}$ (Rhoads 1997, 1999; Sari & Piran 1999). Photon energies from the expanding remnant decrease as Γ decreases, with the net effect that some off-axis events should be seen as "orphan afterglows" without accompanying gamma rays.

In principle, the event rates of both dirty fireballs and off-axis orphan afterglows could greatly exceed the rate of observable GRBs. In practice, preliminary indications from ZTF do not show large numbers of orphan afterglows (Ho et al. 2022).

Ultimately, we would like to study the overall population of relativistic fireballs. Suppose we describe each fireball with its total energy E, collimation angle $\theta_{\rm jet}$, and peak Lorentz factor Γ. We would like to measure the event rate in this multidimensional parameter space $R(E, \theta_{\rm jet}, \Gamma, z)$.

GRB experiments constrain this distribution for $\Gamma \gtrsim 100$, subject to thresholds in fluence or flux. Multiwavelength monitoring of GRB afterglows yields constraints on the distribution of $\theta_{\rm jet}$. ULTRASAT offers the wavelength coverage to probe down to Γ of a few, and the survey efficiency (grasp) to measure values of R that are appreciably smaller than the intrinsic GRB rate.

Full interpretation of the fireball population observed by ULTRASAT will doubtless require more sophisticated physical models than the arguments presented above. Relativistic hydrodynamical simulations (Granot et al. 2018) can be used to examine the light curves expected as a function of wavelength, jet angle, and viewing angle.

5.5. Stars and Stellar Remnants

In the UV range, as in the optical and in the IR, the majority of sources brighter than ~20 mag in an astronomical image, particularly at low Galactic latitudes, are stars and their WD remnants. ULTRASAT's unique combination of a large FOV, a long, continuous, dwell time with a high cadence, and all this in the UV, will open up largely uncharted territories in the study of stars and WDs.

5.5.1. Stellar Rotation and Chromospheric Activity

The link between rotation and magnetic activity in stars can appear in all layers of the stellar atmosphere, be it in the photosphere (e.g., Suárez Mascareño et al. 2016), the chromosphere (e.g., Olmedo et al. 2013; Astudillo-Defru et al. 2017), or the corona (e.g., Wright et al. 2011; Pizzocaro et al. 2019). The manifestations of stellar spots and flares and their connections to magnetic field, stellar age, and rotation have been probed only scantily in the UV, let alone have they been well characterized. Apart from the poorly understood physics underlying these phenomena, observing stellar activity has also gained practical importance for the discovery and characterization of exoplanets. The radial velocity (RV) accuracy achievable using advanced methods and stabilized spectrographs (e.g., Anglada-Escudé et al. 2016) is ultimately limited by the magnetic activity of the host stars, which can cause RV jitter with amplitudes of $\gtrsim$10 m s^{-1} (Tal-Or et al. 2018), and can mask or mimic the signal caused by substellar companions.

To assess quantitatively the amount of magnetic-activity-related emission from normal stars that ULTRASAT will see, we have analyzed archival data from the XMM-Newton (XMM) Optical Monitor (OM; Mason et al. 2001), whose UVM2 filter is similar in width and central wavelength to the ULTRASAT bandpass. Point sources from the XMM-SUSS 4.1 catalog (Page et al. 2012) with a S/N $\geqslant$ 5 in the UVM2 filter were cross-matched with the Gaia DR2 source catalog (Gaia Collaboration et al. 2018) to obtain parallaxes, and with the LAMOST DR5 catalog (Luo et al. 2019) to obtain stellar parameters (log g, [Fe/H], and $T_{\rm eff}$) for a total of 8859 stars. The UV flux measured by the XMM OM consists of photospheric and chromospheric contributions. To estimate the photospheric contribution, we folded each spectrum from the latest PHOENIX stellar atmosphere grid (Husser et al. 2013) through the UVM2 filter transmission function, yielding a grid of theoretical UV fluxes for the full range of surface gravities, effective temperatures, and metallicities. For each star in the XMM OM catalog we then interpolated, on this grid, its theoretical photospheric UV flux. In analogy to the stellar activity indicator R'_{HK}, we define a UV excess index,

$$R'_{\rm NUV} = \frac{f_{\rm UVM2} - f_{\rm phot}}{f_{\rm bol}}, \quad (1)$$

where $f_{\rm UVM2}$ is the flux measured by the XMM OM, $f_{\rm phot}$ is the theoretical photospheric flux in the UVM2 band from PHOENIX, and $f_{\rm bol}$ is the bolometric flux based on Gaia.

Figure 7 shows the nonphotospheric UV flux excess as a function of stellar effective temperature, where the color coding of the points denotes the Gaia/Apsis reddening coefficient $E(BP-RP)$. The red curve shows the $R'_{\rm UVM2}$ of the bottom fifth percentile of all sources with a reddening coefficient $E(BP-RP) \leqslant 0.05$. We see that, for a large majority of all stars, chromospheric emission in the UVM2 band constitutes a nonnegligible fraction, 0.1% to 5%, of the bolometric luminosity of the star, with typical values $\sim$1%–3%, and a clear rising trend with effective temperature. Note that this excess UV flux is accumulated over generally long XMM integrations, and likely consists of both variable and steady-state components. ULTRASAT will thus be ideally positioned to measure and characterize this important component of stars, and its behavior (particularly in the temporal regime).

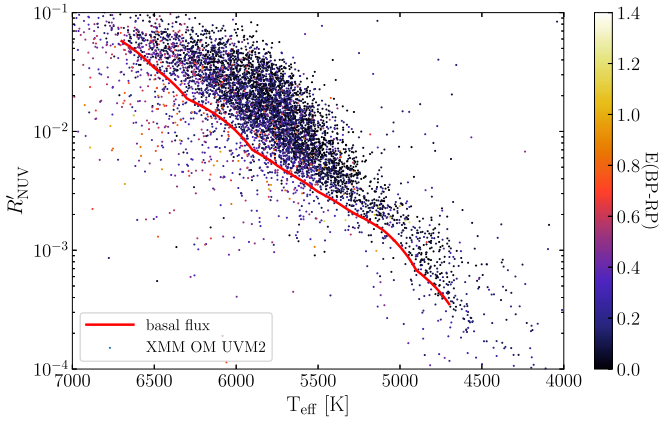

Figure 7. Relative chromospheric flux excess over the model photospheric flux, vs. effective temperature, for 8859 stellar sources observed in the UV with XMM OM, in the Gaia DR2 source catalog and in the LAMOST DR5 catalog. The color coding of the points reflects the reddening. The red line denotes the the flux excess of the bottom fifth percentile of stars having reddening coefficient $E(BP-RP) \leqslant 0.05$.

The magnetic activity of stars manifests itself observationally as variability in two forms: stochastic variability from stellar flares that arise from magnetic instabilities in the chromosphere and the corona and periodic variations resulting from photospheric stellar spots, combined with stellar rotation. The mission-long UV light curves of all stars observed with ULTRASAT will be an unparalleled resource for characterizing both of these types of stellar variability in the UV.

Recent studies have revealed, in growing detail, large-scale trends with stellar properties of the optical variability periods that trace the rotation periods (e.g., McQuillan et al. 2014; Davenport & Covey 2018; Canto Martins et al. 2020; Gordon et al. 2021; Briegal et al. 2022). Apart from an empirical trend between stellar color and rotation period, which permits deducing a star's age ("gyrochronology"—stars lose angular momentum and magnetic field strength as they age), several of these studies and others have shown an intriguing bimodal structure in the parameter space of the rotation periods of main-sequence stars with respect to color, with a dearth of stars in a period gap between $\sim$15 and 25 days. These results have emerged largely from Kepler and TESS data with their continuous, high-cadence, temporal sampling, similar to that planned for ULTRASAT. The ULTRASAT data will permit extending such studies, for the first time, into the UV, with this band's sensitive and independent indicators of magnetic activity. Systematic large surveys of stellar activity are in progress also in X-rays (eROSITA; Merloni et al. 2012). In radio, stellar activity studies require observations based on pointing and dwelling on individual stars, but a large body of data has already been collected (e.g., Crosley & Osten 2018; Villadsen & Hallinan 2019; Vedantham et al. 2020, and references therein). ULTRASAT data will thus be instrumental for intercomparisons of these phenomena across the EM spectrum. Active short-period binaries and planet hosts are another promising category for ULTRASAT studies. The topology of the stellar magnetic field may be modified by the presence of a close companion. The UV emission from the corona, which is in interaction with the magnetic field, should be modulated with the stellar binary period and with the rotation period, assuming the system has reached synchronization via tidal dissipation. If synchronization has not been achieved, the stellar magnetic topology can be complex, with possible induced instabilities that will be reflected in the UV variability observed by ULTRASAT.

In summary, the still poorly understood question of how magnetic activity operates in normal stars will receive a major resource from the characterization by ULTRASAT of UV variability, potentially for a large fraction of all the stars that it will observe. Planned ULTRASAT studies of the stochastic flaring activity (rather than periodic variability) of normal stars are further discussed in Section 5.6.

5.5.2. White Dwarf Accretion and Rotation

Distinct from pulsating WDs (which are on the WD instability regions in the H-R diagram, with periods of minutes), photometrically variable WDs with amplitudes $\sim 10\%$ and periods of hours to months are known, but rare. Except in a few individual cases that may be explained by effects connected to an orbit with a companion mass (beaming, reflection, and ellipsoidal tidal distortion), the variability has been generally associated with WD rotation (which has the same typical range of periods), combined with nonuniform surface emissivity. Except for very cool WDs, most WDs have fully radiative atmospheres, devoid of the convective cells that can produce star spots. The photospheric inhomogeneity implied in variable WDs has therefore been ascribed, instead, to extreme magnetic field strengths that produce magnetic dichroism (Angel et al. 1981).

However, Maoz et al. (2015), analyzing a Kepler time series of 14 normal WDs, found periodic photometric modulations in seven of them. The variation periods were of order hours to 10 days, with amplitudes of order 10^{-4}–10^{-3}, much lower than could have been detected with pre-Kepler technology. This discovery raised the possibility that most or all WDs have low-level variability associated with rotation, but also exacerbated the problem of how to produce, as a rule in WDs, an inhomogeneous WD photosphere. Maoz et al. (2015) and Hallakoun et al. (2018) hypothesized that the optical-band low-level photometric modulation seen in many WDs could be associated with photospheric metal pollution, which is likewise seen in a large fraction of WDs (Koester et al. 2014).

Over the past couple of decades it has become widely accepted that the optical and UV metal absorption lines seen in WD atmospheres are the result of ongoing accretion of planetary debris onto the WD (Jura 2003; Zuckerman et al. 2003, 2010; Gänsicke et al. 2012; Koester et al. 2014). Slightly inhomogeneous surface coverage of the accreted material (e.g., due to moderate magnetic fields) could lead to inhomogeneous UV absorption. Optical fluorescence of the absorbed UV photons (Pinto & Eastman 2000), combined with the WD rotation, could then potentially produce the observed levels and periods of optical modulation.

We estimate that ~400 WDs will be detected above the limiting magnitude in every ULTRASAT field. Although the 10^{-4}–10^{-3} variation amplitudes seen with Kepler will be near the limit detectable with ULTRASAT (depending on the level of hard to foresee systematics), many WDs show modulations with larger amplitudes, mostly in optical-band photometric surveys (such as Kepler's K2 continuation mission). One example of a high-amplitude UV-variable WD is GD 394. This hot, metal-polluted WD was observed in the past by the Extreme Ultraviolet Explorer and displayed 25% variations in the extreme-ultraviolet (70–380 Å) with a period of 1.15 days (Christian et al. 1999; Dupuis et al. 2000). Follow-up far-ultraviolet (FUV) spectroscopy (1144–1710 Å) taken in 2015 with HST failed to detect any variability, down to the 1% level (Wilson et al. 2019). However, recent TESS data have revealed 12% amplitude optical variations, with a similar period (Wilson et al. 2020). GD 394 has some striking similarities to WD J1855+4207 (Maoz et al. 2015; Hallakoun et al. 2018). Both are hot ($\gtrsim$30,000 K) WDs with indications of highly ionized circumstellar metals, in addition to the detected photospheric metals, and both have relatively large periodic optical modulations. The monitoring of the numerous WDs in the ULTRASAT-monitored fields can potentially detect additional such large-amplitude or changing-amplitude WDs.

Furthermore, in the case of a WD with significant metal pollution in its photosphere, UV variability over short (minutes to days) or long (months to years) timescales, could indicate a change in the debris accretion rate, or in the structure of the circumstellar debris around the WD. Combined with simultaneous photometric monitoring in multiple bands (from the UV to the NIR) using ground-based facilities (e.g., Hallakoun et al. 2017; Xu et al. 2019), ULTRASAT may thus finally provide answers to the question of how periodic variability is produced in a large fraction of WDs.

5.6. Exoplanets and the Star–Planet Connection

The discovery of thousands of extrasolar planets ranks among the most exciting scientific developments of the past decades. ULTRASAT capabilities allow us to explore unique regions of exoplanet and star–planet connection parameter space. In this section we focus on two research topics that ULTRASAT will significantly advance—host activity (Section 5.6.1) and the search for planets around WDs (Section 5.6.2). We also discuss ULTRASAT's potential to study exoplanet atmospheres (Section 5.6.3), albeit this will require modifying the survey modes.

5.6.1. Planet's Host activity

The UV radiation emitted from a host star on an orbiting planet can dictate whether a planet retains its atmosphere, and govern the photochemistry in it. In addition, the UV flux will have both positive and negative contribution to the likelihood of life developing on it (Buccino et al. 2006; Ranjan & Sasselov 2016). As a stressor, high fluxes of UV radiation, in either steady-state emission or through flares, can destroy nascent biomolecules through photolysis. As a eustressor, recent studies indicate UV radiation can play a key role in prebiotic chemistry, and might have been the most abundant energy source on the young Earth. In the context of the search for biologic activity, UV emission can result in abiotic generation of bona fide biosignatures, such as the disassociation of water molecules in exoplanets orbiting dM stars that will in turn result in a high concentration of molecular oxygen (Meadows et al. 2018). Therefore, one must know the UV radiation field around a planet to understand its atmosphere evolution. Defining an ultraviolet habitable zone (UV HZ)—the range of orbits in which the UV radiation from the host star will allow (and contribute) to the evolution of life as we know it—is critical for putting the evolution of life on our own planet on a Galactic scale, and for the search of bioactivity on other worlds.

Despite the impact of UV radiation on exoplanet atmosphere evolution and the likelihood of bioactivity, our understanding of the UV emission from stellar objects is limited, and the commonly used photospheric models routinely underestimate

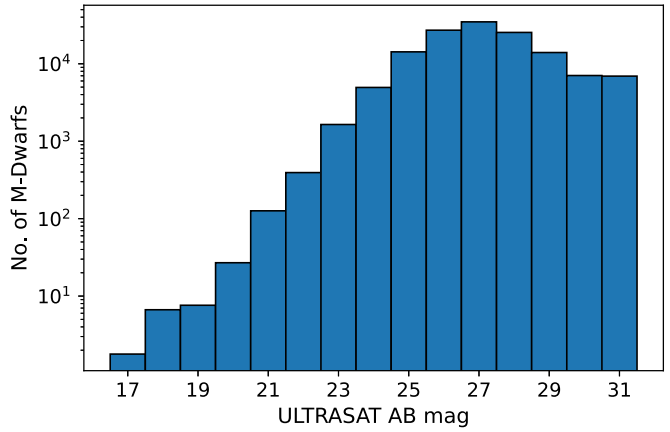

Figure 8. Magnitude distribution of dM stars in quiescence up to 800 pc in an exemplar ULTRASAT FOV. While flaring they can get up to ∼5 mag brighter (Rekhi et al. 2023). Input catalogs used include the TESS Input Catalog (Stassun 2019). The limiting magnitude for a three-image coadd for dM stars is ≈21.4.

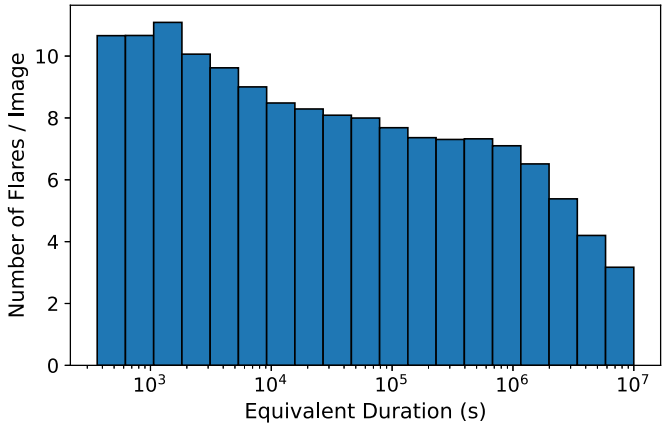

Figure 9. The expected distribution of flares detected in each 300 s ULTRASAT image, for the the dM population shown in Figure 8. The high-energy tail of the distribution, with equivalent duration $\geqslant 10^4$ s, is poorly constrained. A Monte Carlo simulation in which the NUV FFD was empirically derived from GALEX observations suggests each ULTRASAT image will capture ∼150 flares from dM stars (Rekhi et al. 2023).

it, as the UV emission for, e.g., dM stars, originates in the chromosphere and transition region (France et al. 2013). Our current capability to characterize it for various stellar types is hindered by the small number of UV observatories to date, the lack of large UV data sets, and the large variance in the UV radiation in both short- and long-duration scales, i.e., flares for the former and variability for the latter.

Initial studies performed with the limited data available are portraying a complicated picture, specifically for dM stars, the most common stars in the solar neighborhood and preferred targets for many exoplanet transit searches due to favorable planet-to-host radius ratios, and the potential for atmosphere studies. Some suggest that the HZ and the UV HZ do not necessarily coincide for various stellar types (Buccino et al. 2006). Another study using HST data indicates that some dM stars that seem to be in a quiescent state when observed in the visible band are active in the UV band (France et al. 2016). These results demonstrate clearly the need for a detailed study of UV radiation from a large sample of stars of various stellar types. Additional data, albeit for a limited sample, is expected from two CubeSats missions that have recently been launched: the Colorado UV Transit Explorer (Fleming et al. 2018) and the Star–Planet Activity Research CubeSat (SPARCS; Ramiaramanantsoa et al. 2022).

The total number of stars within the ULTRASAT FOV and up to ∼800 pc is estimated to be ≈200,000, with roughly half of them being dM stars, see Figure 8. For the latter in quiescence, we expect to detect only O(1–10) stars for coadds of three images, and $O(10^3)$ stars for coadds reaching an estimated confusion limit of 24 mag in the ULTRASAT wave band. Assuming the NUV flare frequency distribution (FFD) derived by Rekhi et al. (2023) using archival GALEX data, each 300 s ULTRASAT image will capture ∼150 flaring dM stars, with the equivalent duration distribution shown in Figure 9, for which ≈50% of the flares are in the poorly constrained high-energy regime. The distributions shown in Figures 8 and 9 demonstrate how the long-baseline observations of ULTRASAT will allow us to monitor the high-energy tail of the FFD (i.e., equivalent duration $\geqslant 10^4$ s), which is poorly constrained to date. Flares in this energy range are expected to have a significant effect on exoplanet atmospheres. The data will provide us a more complete picture of the high-energy radiation environment around stellar hosts, and will allow us to determine the best candidates for expensive spectroscopic studies of exoplanet atmospheres by, e.g., JWST and the upcoming extremely large telescopes.

5.6.2. *Planets around White Dwarfs*

Occurrence rate studies show that most main-sequence stars host exoplanets (Cassan et al. 2012; Winn & Fabrycky 2015). The vast majority of these hosts will evolve into WDs. Planets in close orbits are unlikely to survive this transition, as the host star climbs the red giant branch and its envelope expands. Despite the expected fate of close-in planets, both direct and indirect evidence have been accumulated for the presence of substellar objects and minor bodies in close orbit around WDs (Veras 2021). Several explanations for the presence of these objects have been suggested. Planets can be captured and/or migrate from wide orbits into close orbits after the host transition into a WD is completed (Debes & Sigurdsson 2002). Planets can also form out of gas near the WD, e.g., via the interaction or merger of binary stars (i.e., second-generation planets; Livio et al. 2005). Studying the occurrence rates of planets around WDs can shed light on the evolution of these systems. Moreover, given the slow change in the flux emitted by a WD as it ages, the continuous habitable zone (CHZ) around a WD can have a lifetime of $\gtrsim$3 Gyr for orbital periods ≈4–32 hr (Agol 2011). Planets detected in the CHZ will be optimal for atmosphere studies and searches for biomarkers in their transmission spectra (Loeb & Maoz 2013).

The search for planets around WDs is a rapidly growing field, with a few detections of both disintegrating planets or planetesimals, and a transiting giant planet candidate (e.g., Vanderburg et al. 2020; see the review by Veras 2021). Due to the small radii of WDs, the transit depth induced by a planet is large and can be detected with standard photometric precision telescopes (e.g., ground-based and ULTRASAT), making transit detection possible despite WDs being faint compared to typical targets of exoplanet surveys. Currently, all occurrence rate constraints are based on null detections (thus giving only upper limits). Fulton et al. (2014) used a sample

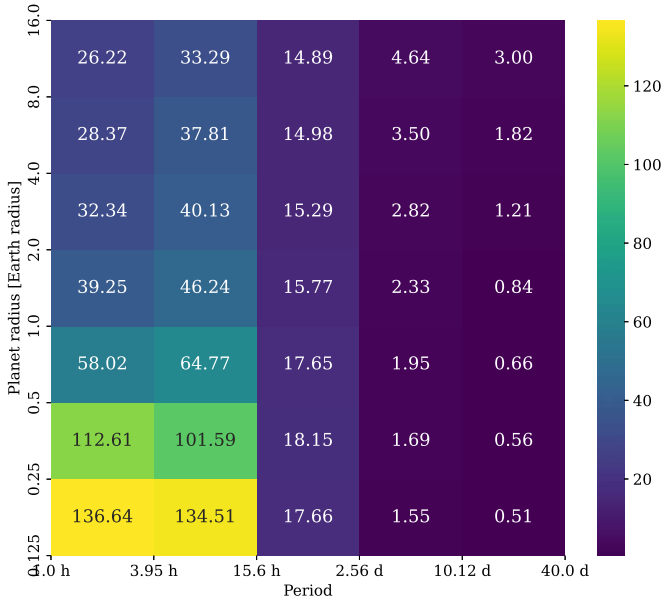

Figure 10. Maximum number of WD-transiting planets detected by ULTRASAT, by both the low-cadence survey and high-cadence survey. Based on the current occurrence rate upper limits from van Sluijs & Van Eylen (2018).

~1700 WDs observed by the Pan-STARRS survey to constrain planet occurrence rates in the HZs of WDs. They find an occurrence upper limit of 3.5% for $R_{\rm pl} = 2$–$5\ R_{\oplus}$, but cannot constrain the occupancy rate for planets with smaller radii. van Sluijs & Van Eylen (2018) investigated the light curves of 1148 WDs from Kepler's K2 campaign, and conclude that the occurrence of habitable Earth-sized planets ($R_{\rm pl} = 1$–$2\ R_{\oplus}$) around WDs is <28%, approximately equal or less than their main-sequence occurrence. A key to move forward is to increase significantly the number of monitored WDs. ULTRASAT, with a large FOV that can image hundreds of WDs in a single exposure, is ideal for this task.

The number of WD-transiting planets is given by,

$$N_{\rm WD,pl} = N_{\rm WD} f_{\rm WD,pl}\, P_{\rm transit}\, P_{\rm detection}, \quad (2)$$

where $N_{\rm WD}$ is the total number of monitored WDs, $f_{\rm WD,pl}$ is the fraction of WDs hosting planets with orbital period $< P$, $P_{\rm transit}$ is the transit probability, $(R_{\rm pl} + R_{\rm WD})/a$, and $P_{\rm detection}$ is the probability to detect at least $N_{\rm tr}$ transits. The ULTRASAT low-cadence survey will monitor $N_{\rm WD} \approx 32{,}000$ WDs (40 fields in each hemisphere, 400 WDs per field), an order of magnitude larger than previous studies (see Ben-Ami et al. 2023 for a future planned survey). In addition, ~800 WDs will be monitored by the ULTRASAT high-cadence survey each year.[26] The detection probability, assuming the transit can be detected in a single visit, is,

$$P_{\rm tr,det} = 1 - \sum_{k=0}^{N_{\rm tr}-1} \binom{n_{\rm vis}}{k} \left(\frac{t_{\rm vis}}{P}\right)^{k} \left(1 - \frac{t_{\rm vis}}{P}\right)^{n-k}, \quad (3)$$

where $n_{\rm vis}$ is the number of visits and $t_{\rm vis}$ is the duration of each visit. The low-cadence survey fields cover almost all of the low-extinction ($A_{\rm ULTRASAT} < 1$) sky in each hemisphere. Thus, for our current calculations we assume these will be the same fields for the entire 3 yr mission. Under this assumption, the low-cadence survey will have ~135 visits per field, each of $t_{\rm vis} = 15$ minutes. The high-cadence survey fields will have over 45,000 images each year.

We use the 68% upper limits on $f_{\rm WD,pl}$ from van Sluijs & Van Eylen (2018) to estimate the maximal number of WD-transiting planets with at least $N_{\rm tr} = 3$ detected transits by ULTRASAT, for a range of planet radii and orbital periods (Figure 10). We find that ULTRASAT is highly sensitive to planets in the entire CHZ, with the maximal number of detected planets well over 100 (assuming occupancy rates identical to the upper limits derived by van Sluijs & Van Eylen 2018). The high number of detections is a result of the large sample of WDs monitored by the low-cadence survey. ULTRASAT will thus be able to deliver significantly tighter upper limits to those available from any other existing survey, or better yet, will deliver a unique sample of planets and minor bodies in short orbits around WDs. Planets at wider orbits than the CHZ can also be detected (mainly via the high-cadence survey), but with a smaller statistical impact.

5.6.3. Exoplanet Atmospheres

The NUV bandpass holds unique prospects for the study of exoplanet atmospheres (e.g., Christian et al. 1999). Several studies show the potential of NUV observations to differentiate between atmosphere models, as this wavelength range contains telltales for the presence of clouds and haze (Goyal et al. 2018). In addition, an escaping atmosphere will result in deeper transits in the NUV, as the optical depth of the escaping atmosphere is higher at shorter wavelengths (e.g., Vidal-Madjar et al. 2013; Salz et al. 2019). While the cases above are typically targeted by FUV measurements, as the signature is expected to be intrinsically stronger at this band, the NUV bandpass hold several unique advantages (e.g., Christian et al. 1999), mainly the uniform distribution of NUV emission across the stellar disk when compared to the FUV—which makes the scientific derivation more secure—and the reduced stellar attenuation in the NUV bandpass relative to the FUV. It is not clear whether ULTRASAT will deliver the precision needed for such studies. As a starting point and capability demonstration, ULTRASAT will attempt to detect the signature of escaping atmosphere from several bona fide examples, such as WASP-12b. The signature of the escaping atmosphere in these cases is several millimagnitudes (Fossati et al. 2010), well within the instrument capabilities, see Figure 6. These cases will allow us to establish the precision limits of the instrument and will allow us to plan a dedicated survey for, e.g., the search for escaping atmospheres from exoplanets in short orbits. We emphasize that the science case described in this section is not a part of the standard survey, and will require several changes to the standard observing strategy, such as changes in the exposure time.

5.7. Tidal Disruption Events

TDEs offer a novel probe of massive black hole (MBH) demographics, super-Eddington accretion physics, and stellar dynamics in galactic nuclei. Theoretical dynamics calculations indicate that the volumetric TDE rate should be dominated by the smallest galaxies with a high MBH occupation fraction (Wang & Merritt 2004; Stone & Metzger 2016), indicating that statistical samples of TDEs can resolve open questions about

[26] We assume that the high-cadence fields will be different each year, though this is still to be decided.

the poorly understood low end of the MBH mass function (Greene et al. 2020). As probes of MBH demographics, TDEs have the unique ability to sample quiescent galactic nuclei to cosmological distances (Bloom et al. 2011; Chornock et al. 2014), and perhaps to measure MBH spins (Stone & Loeb 2012; Guillochon & Ramirez-Ruiz 2015; Wen et al. 2020) as well as masses (Rees 1988; Mockler et al. 2019; Ryu et al. 2020). There are indications that TDEs may be multimessenger sources, as two different high-energy IceCube neutrinos have been temporally and spatially coincident with TDE flares (Stein et al. 2021; Reusch et al. 2022). More speculatively, TDEs may be linked to LISA-band GW sources, either preceding (Seto & Muto 2011) or following (Stone & Loeb 2011) the GW signal from a merging MBH binary, and may even lead to novel tests of fundamental physics (Lu et al. 2017; Wen et al. 2021).

A TDE is set in motion when a star is scattered onto a highly radial orbit (Frank & Rees 1976) around a MBH of mass $M_\bullet$. Once its pericenter R_p passes within the tidal radius $R_t \approx R_\star (M_\bullet/M_\star)^{1/3}$, the star is disrupted (Hills 1975; Rees 1988). Half of the stellar debris eventually returns on highly eccentric ($e \gtrsim 0.99$) but bound orbits, powering a highly luminous flare. While the hydrodynamic evolution and radiative emission processes in TDEs remain highly uncertain and hotly debated (see Roth et al. 2020; Bonnerot & Stone 2021, for recent reviews), the last decade of detections has shown that typical TDEs are blue, quasi-thermal transients of high luminosity (Gezari et al. 2008a; van Velzen et al. 2011; Gezari et al. 2012; Arcavi et al. 2014). Typical peak bolometric luminosities range from $L_{BB} \sim 10^{43-44.5}$ erg s^{-1}; typical blackbody temperatures range from $T_{BB} \approx 2$–4×10^4 K, and there is little color evolution over timescales of weeks to months (Hung et al. 2017; van Velzen et al. 2021). Despite their high luminosities, TDEs are challenging to discover because of their low event rate, which is likely $\dot{N}_{TDE} \sim 10^{-4}$ galaxy^{-1} yr^{-1} (Stone & Metzger 2016; van Velzen 2018), about 1% of the core-collapse SN rate.

The high effective temperatures and low volumetric rates of TDEs make them ideal targets for ULTRASAT, given the mission's large grasp and UV sensitivity. In contrast to other transients of interest for ULTRASAT (e.g., shock breakout), TDEs evolve slowly, over timescales of days to weeks (Gezari et al. 2012; Arcavi et al. 2014; Hung et al. 2017), and therefore will benefit from the low-cadence survey mode.

We now quantify the number of TDEs that ULTRASAT will detect and identify every year. We emphasize in advance that these estimates are quite approximate and incorporate significant assumptions on TDE flare populations as well as unavoidable ambiguities in what counts as a secure identification.

We crudely estimate the limiting luminosity distance for detecting a TDE,

$$D_L^{max} = \sqrt{\frac{L_{\nu,peak}}{4\pi F_{\nu,lim}}}, \quad (4)$$

where $L_{\nu,peak}$ is the peak UV luminosity density of a TDE and $F_{\nu,lim}$ is the limiting flux density of ULTRASAT. If we consider a fiducial TDE with a single-temperature blackbody spectrum, an effective temperature (at peak) $T = 2 \times 10^4$ K, and peak (bolometric) luminosity $L_{peak} = 10^{44}$ erg s^{-1}, then the peak luminosity density at the center of the ULTRASAT band (250 nm) is $L_{\nu,peak} = 5.2 \times 10^{28}$ erg s^{-1} Hz^{-1}. Considering the low-cadence survey mode with a typical limiting AB magnitude of $m = 22.5$, the UV detection horizon will be cosmological in distance, so we include K-corrections, and find that $D_L^{max} \approx 3$ Gpc, or $z^{max} \approx 0.6$.

Since TDEs show minimal UV brightness evolution over the course of a few days (see van Velzen et al. 2020; Gezari 2021, and references therein), neither survey mode will be cadence limited, and the number of TDEs found in a single survey of duration ΔT and sky coverage $\Delta\Omega$ will be,

$$N \approx \frac{\Delta\Omega}{4\pi}\Delta T \int_{L_{min}}^{L_{max}} dL_{peak} \int_0^{D_L^{max}(L_{peak})} dD_L \times 4\pi D_L^2 (1+z)^{-3} \frac{d\dot{n}}{dL_{peak}}. \quad (5)$$

Here the extra factor of $(1+z)^{-3}$ converts to an integral over comoving distance. In the following rate calculations, we will estimate the total number of TDEs N found during a survey of $\Delta T = 1$ yr, considering both the low-cadence and high-cadence modes of operation. For the low-cadence survey, we take a limiting AB magnitude of $m_{low} = 22.5$ for detection. For the high-cadence survey, we assume that individual exposures can be coadded over the course of a single day to increase detection sensitivity. As $m = 22.5$ was the limiting magnitude for a set of exposures with total duration 900 s, we estimate the limiting magnitude for a detection using 21 hr of stacked observations as $m_{high} = m_{low} + (5/4)\log_{10}(75600/900) \approx 24.9$. However, ULTRASAT fields will typically be confusion limited at magnitudes $m > m_{conf} \approx 23.5$, so we conservatively assume any TDEs dimmer than m_{conf} will not be found.

We will approximate the volumetric (and bolometric) TDE luminosity function as,

$$\frac{d\dot{n}}{dL_{peak}} = \dot{n} \times \frac{dN}{dL_{peak}}, \quad (6)$$

where $\dot{n}$ is the volumetric TDE rate, and,

$$\frac{dN}{dL_{peak}} = 1.5 \frac{L_{peak}^{-2.5}}{L_{min}^{-1.5} - L_{max}^{-1.5}}. \quad (7)$$

This is the empirical bolometric optical/NUV luminosity function fitted by van Velzen (2018), where L_{min} is the unknown bottom end of the luminosity function and $L_{max} \approx 10^{45}$ erg s^{-1} (Leloudas et al. 2016; van Velzen et al. 2021; Reusch et al. 2022). Based on our current flux-limited sample, $L_{min} \lesssim 10^{42.5}$ erg s^{-1}; as these faint TDEs will dominate the total volumetric event rate, we set $L_{min} = 10^{42.5}$ erg s^{-1} as a conservative choice. For simplicity, we will convert bolometric luminosities into UV magnitudes by assuming that every TDE is a blackbody of constant temperature T_{BB}, although we consider three different cases: $T_{BB} = \{2, 3, 4\} \times 10^4$ K.

A final assumption that enters our calculation concerns the volumetric TDE rate $\dot{n}(z)$. At low redshift, we take $\dot{n}(0) = 3 \times 10^{-6}$ Mpc^{-3} yr^{-1} (the most conservative choice from the rate calculations of Stone & Metzger 2016; and a result in reasonable agreement with the volume-corrected empirical analysis of van Velzen 2018). However, the redshift evolution of this rate is almost completely unknown. Theoretical

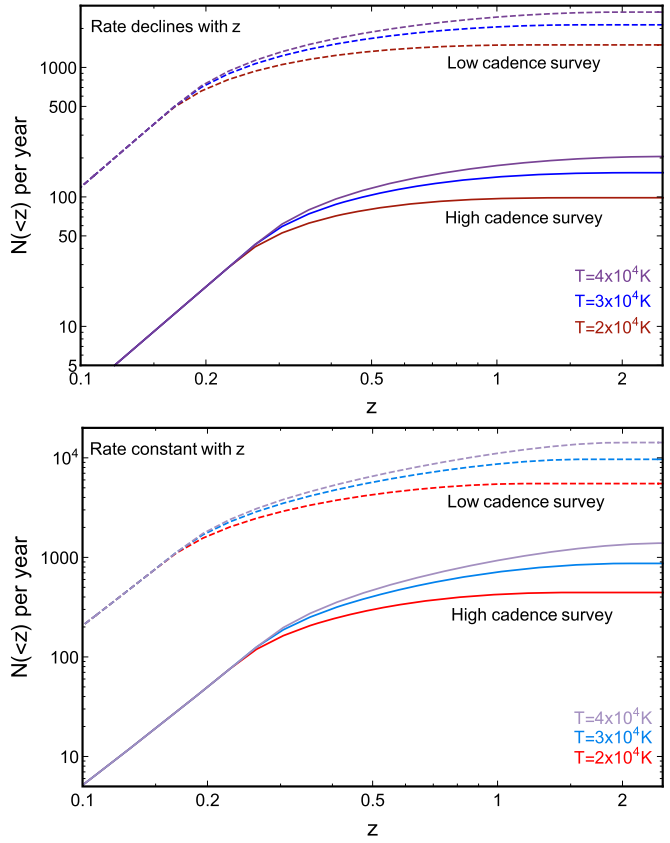

Figure 11. The cumulative number of TDEs detected per year within a given redshift, $N(<z)$. Colors show the effective blackbody temperature T of the TDE spectra at peak; we consider the idealized cases of $T = 2 \times 10^4$ K (red), $T = 3 \times 10^4$ K (blue), and $T = 4 \times 10^4$ K (purple). The detection rates are shown assuming a volumetric rate that declines steeply with z (top panel, dark colors) or one that is constant with z (bottom panel, light colors). In these rate calculations, we consider both the high-cadence (solid lines) and low-cadence (dashed lines) survey modes. In the low-cadence calculations, we count as a "detection" every TDE with a peak magnitude $m \leqslant 22.5$, while in the high-cadence calculations, we assume faint exposures over the course of 1 day are coadded up to a confusion limit of $m = 23.5$.

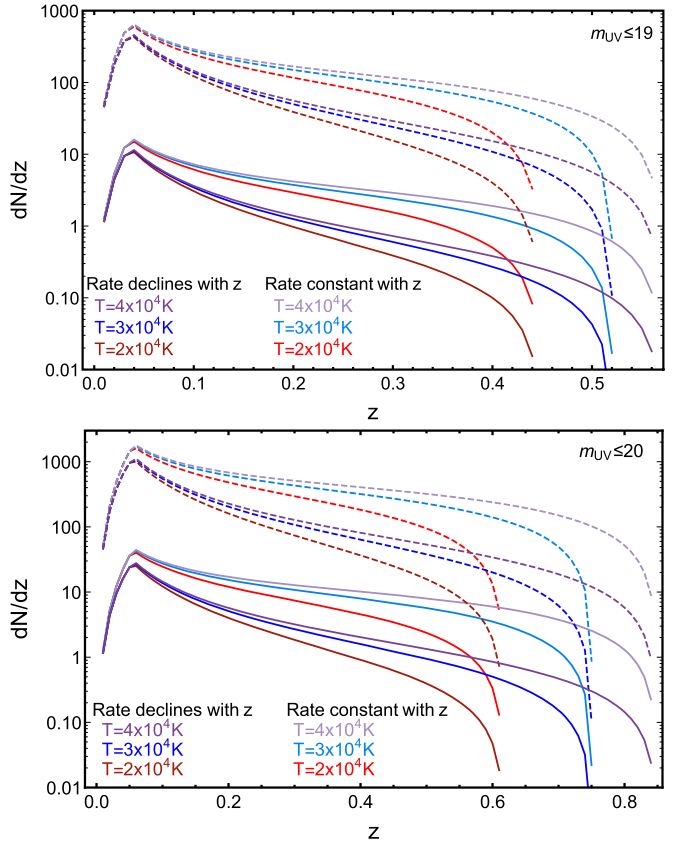

Figure 12. The differential number of TDEs suitable for spectroscopic follow up detected per year around a certain redshift, dN/dz. The line styles and colors are the same as in Figure 11, except that we now only count TDEs with peak UV magnitude $m \leqslant 19$ (top panel) or $m \leqslant 20$ (bottom panel). This restriction greatly reduces the maximum redshift out to which ULTRASAT will find TDEs of interest, and represents a factor $\sim$ 50–150 reduction from the total number of detected TDEs (for the $m \leqslant 19$ case).

calculations (Kochanek 2016) suggest that if $\dot{n}$ tracks the volume density of SMBHs, it will decline steeply with redshift. We consider as an optimistic case $\dot{n}(z) = \dot{n}(0)$, and as a pessimistic case, $\dot{n}(z) = \dot{n}(0)/(1 + 10z)$, which crudely approximates the results of Kochanek (2016).

The results of our approximate rate calculations are presented in Figure 11, which shows the cumulative number of TDEs found below a certain redshift. For the most pessimistic combination of assumptions ($T_{\rm BB} = 2 \times 10^4$ K and $\dot{n}(z)$ declines with z), the high-cadence survey will detect $N \approx 100$ TDEs per year and the low-cadence survey $N \approx 1500$. For the most optimistic combination of assumptions ($T_{\rm BB} \approx 4 \times 10^4$ K and $\dot{n}(z)$ independent of z), the high-cadence survey will detect $N \approx 1400$ TDEs per year and the low-cadence survey $N \approx 14{,}000$.

These detection rates are enormous, and dwarf the current sample of a few tens of TDEs (van Velzen et al. 2020). Of course, the number of events that can be classified as TDEs via photometric and spectroscopic follow up will be smaller, perhaps drastically so. This number depends on the limiting magnitude of available follow-up facilities. With commonly available follow-up resources, we will be able to follow dozens of TDEs spectroscopically at or brighter than 19 mag. A smaller number of spectroscopic instruments will be able to follow targets peaking at $m \leqslant 20$. We repeat our calculations using these two limiting magnitudes (19 and 20) for both the low- and high-cadence fields. The results are shown in Figure 12. When $m \leqslant 19$ is used as the relevant threshold, the low-cadence survey will find $N \approx 32$–88 suitable TDEs per year across our range of temperature and redshift assumptions, while the high-cadence survey will struggle to find a single one ($N \approx 0.8$–2.2). When $m \leqslant 20$ is used, the low-cadence survey will find $N \approx 103$–383 suitable TDEs per year, and the low-cadence survey will find $N \approx 2.6$–9.6. These rate estimates could be optimistic by a factor of a few if the true TDE rate is somewhat lower than assumed, as was suggested by a recent ZTF analysis (Yao et al. 2023).

ULTRASAT will not be the only active wide-field survey searching for TDEs. At present, the leader in TDE discovery is the ZTF optical survey, which detects $\approx$20 new flares per year (van Velzen et al. 2021), although the eROSITA X-ray instrument, which has so far found a comparable number (Sazonov et al. 2021), may ultimately be more productive once a longer temporal baseline is established for this low-cadence survey (Khabibullin & Sazonov 2014; Jonker et al. 2020). In the near future, the LSST optical survey will detect thousands of new TDEs every year (van Velzen et al. 2011), but only a small minority of these will actually be identified as TDEs from LSST photometry alone, perhaps as few as 5%–10% (Bricman

& Gomboc 2020). Both the cadence limitations of eROSITA and the wavelength limitations of LSST can potentially be ameliorated by contemporaneous ULTRASAT coverage of the same fields. Likewise, the multiwavelength photometry from these other surveys may help to secure a TDE identification for the more marginal ULTRASAT detections ($m \approx 22.5$), which are inaccessible to spectroscopic confirmation yet nevertheless dominate the raw detection rate. Joint ULTRASAT–optical detections will also be highly valuable for identifying nuclear transients, a task that will be challenging for ULTRASAT-only detections given resolution limitations.

5.8. Active Galactic Nuclei

The radiation emitted from the central engines of AGNs, powered by accretion onto SMBHs, is known to vary on all timescales probed, and to peak in the UV regime. Assuming the canonical geometrically thin, optically thick accretion disk framework, ULTRASAT will be probing the inner parts of AGN accretion disks (tens to hundreds of gravitational radii) down to dynamical timescales ($\sim$10 hr or less; see Stern et al. 2018; Trakhtenbrot et al. 2019a, and references therein for scaling relations). It will also allow to understand better the phenomena that arise from the reprocessing of this "seed" UV radiation in the circumnuclear gas regions gravitationally bound to the accreting SMBH.

ULTRASAT is expected to probe significantly large samples of AGNs, thanks to its wide FOV and high sensitivity, combined with the steep redshift evolution of the AGN luminosity function. Specifically, at the typical ULTRASAT depth of NUV $\simeq$ 21.5 AB mag in a single 3×300 s visit (for $S/N = 10$; see Figure 6), the sky density of unobscured (broad-line) AGNs is expected to reach $\gtrsim$70 deg^{-2}. This (somewhat conservative) estimate is based on the g-band number counts of confirmed broad-line AGNs out to $z \approx 2$ (e.g., Richards et al. 2005) and assuming a canonical SED shape of $f_\nu \propto \nu^{-1/2}$ (Vanden Berk et al. 2001), which yields NUV $\simeq g + 0.32$ (neglecting additional foreground extinction). Thus, every ULTRASAT pointing/FOV is expected to include several thousands of UV-detectable AGNs. Many of these, and particularly the brighter ones, will be previously known spectroscopically confirmed quasars (i.e., from the various Sloan Digital Sky Survey (SDSS) projects, including SDSS-V in the Southern Hemisphere; Kollmeier et al. 2017).

Below we briefly describe some of the main AGN-related science cases for ULTRASAT.

To enable some of these research efforts we plan to pursue follow-up observations in the optical regime using several facilities. This includes (robotic) spectroscopy, using the Las Cumbres Observatory 2 m telescopes (Sand et al. 2011), and narrow/medium-band imaging using a new telescope under construction at Wise Observatory (>15 filters with widths $\sim$100–400 Å) as well as the Panchromatic Array for Survey Telescopes (PAST; E. O. Ofek et al. 2024, in preparation).

5.8.1. Stochastic Variability of Persistent Active Galactic Nuclei

Multiepoch imaging surveys of large AGN samples provide a phenomenological description of their variability, most commonly expressed through the structure function (SF) or the complementary power spectrum distribution (PSD). Persistent AGNs generally vary by $\sim$10% over a year, and show greater (lesser) variability on longer (shorter) timescales. Moreover, the variability amplitude is anticorrelated with luminosity (at a given timescale), and there is ambiguous evidence for trends with other properties (e.g., Vanden Berk et al. 2004; Wilhite et al. 2008; Caplar et al. 2017).

UV variability is known to be higher compared to the optical regime (e.g., Meusinger et al. 2011; Hung et al. 2016; Caplar et al. 2017), and it is key to probing the inner parts of the accretion disks that power AGNs (particularly on short timescales). Our current understanding of short-timescale UV variability in AGN is, however, rather limited. ULTRASAT will provide almost continuous observations, with timescales of minutes to months (4.5 orders of magnitude in timescale) of a large sample of quasars with high S/N (see above). This will allow us to pursue the following studies, among others.

Quantifying active galactic nucleus UV variability on short timescales. ULTRASAT will survey the (nearly) uncharted territory of short-timescale variability of "normal," persistent AGNs (minutes to days). This would allow one to quantify the full distribution of AGN variability in this crucial regime, and to search for links with basic SMBH properties, such as BH mass, accretion rate ($L_{\rm AGN}$ or $L/L_{\rm Edd}$), radio jet activity, etc., to yield insights for accretion flow models.

Specifically, we will be able to construct the ensemble SF (and PSD) of various groups of AGNs, on all accessible timescales and drawing from all ULTRASAT surveys. The shortest timescales (minutes to hours) are of particular interest, as explained below. We will be able to compare the resulting SF to what is known from the optical regime, and specifically test whether the phenomenological (damped) random walk model, which was suggested to describe AGN variability in the optical regime, is applicable to the UV regime. The ensemble SF and PSD can be also constructed in bins of $L_{\rm AGN}$, $M_{\rm BH}$, and $L/L_{\rm Edd}$, to search for correlations with any of these properties. This, in turn, can be directly used to test various models for accretion disk instabilities (see, e.g., Arévalo & Uttley 2006; Ruan et al. 2014; Caplar et al. 2017). Understanding the full distribution of variability is also important for our ability to identify and quantify "extreme" variability and/or AGN-related transients (see Section 5.8.3).

Black hole mass from a break in the power spectrum. Observations suggests that AGN variability is well described by a PSD with a steep power-law index (e.g., Caplar et al. 2017; Smith et al. 2018, and references therein). In principle, this power law should have both high-frequency ("inner") and low-frequency ("outer") breaks. Since the timescales in the disk scale with the distance from the central BH, the inner break in the PSD may reflect the innermost radius of the accretion disk, which in turn scales linearly with BH mass. Thus, if a high-frequency break in the PSD of AGNs, and its correlation with $M_{\rm BH}$, are established, this may provide a new tool to estimate BH masses in distant systems (and perhaps even probe BH spin).

Measuring this inner break likely requires high-precision continuous UV observations, as the UV radiation is emitted from the innermost parts of the disk (see Springer & Ofek 2021a). Even in the event that an inner break is found, but it is not correlated with BH mass, it may provide new information on the accretion physics in AGNs. Unlike previous studies that focused on the PSD of corona-reprocessed X-ray emission (Kelly et al. 2013), ULTRASAT would focus directly on the inner disk itself, exploring a much broader range of frequencies and possibilities.

5.8.2. Agile Reverberation Mapping

The basic premise of RM in AGN is to map the physical structure of and around the central engine by measuring time lags between variations in the "seed" (UV-dominated) radiation coming from the inner accretion disk, and the reprocessed radiation arising from various circumnuclear gaseous regions (see the recent review by Cackett et al. 2021). These mainly include the (outer) disk itself and the BLR, but also the dusty "torus" (via NIR RM; e.g., Minezaki et al. 2019), or the X-ray-emitting corona (e.g., Kara et al. 2016).

All RM efforts face the same two key practical challenges. First, most campaigns focus on the optical regime, while the seed disk radiation is UV dominated. This practical choice complicates the measurement with (persistent) host emission, and perhaps other reprocessing components (e.g., Chelouche et al. 2019; Vincentelli et al. 2021; Netzer 2022). Second, monitoring a sizable AGN sample for a long period and a sufficiently high cadence is extremely challenging, although it is clearly required to ensure that significant variability in both the seed (disk) and responsive emission components is properly recorded. Photometric RM alleviates some of these practical challenges, as it allows one to measure AGN time lags robustly through photometric monitoring with various band widths instead of spectroscopy, as demonstrated by a growing number of studies (see, e.g., Chelouche & Zucker 2013; Chelouche et al. 2014; Ramolla et al. 2018; Kim et al. 2019b; Kovačević et al. 2022; Pozo Nuñez et al. 2023, and additional references below).

ULTRASAT will allow us to make great progress in AGN RM studies. It will continuously monitor the NUV emission of hundreds to thousands of luminous AGNs, which is completely dominated by accretion disk radiation. The nearly real-time data processing would ensure that follow-up observations can be efficiently carried out, i.e., only when significant changes to the seed UV emission are detected. Similarly, NIR or X-ray imaging can be triggered to study the dusty torus or the corona (respectively).

Broad-line region reverberation mapping. RM of broad emission lines in (unobscured) AGNs allows one to study the structure and physics of the BLR (Peterson 1993). The time lag, and thus size measurements, of this dense circumnuclear gas ($R_{\rm BLR}$; Kaspi et al. 2000; Bentz et al. 2013), combined with measurements of its virialized, SMBH-governed kinematics, provide a way to estimate $M_{\rm BH}$ for huge samples of distant AGNs (out to $z > 6$; e.g., Trakhtenbrot & Netzer 2012). To date, reliable BLR lags were measured for several tens of AGNs (e.g., Bentz & Katz 2015; Homayouni et al. 2020; Yu et al. 2023, and references therein). The most recent optical studies demonstrate the difficulty in expensive monitoring of sources that do not exhibit sufficient variability and the significant scatter in the optical L–$R_{\rm BLR}$ relation, which may be alleviated if the UV continuum is monitored instead.

The typical BLR sizes of several light-days to light-months mean that the few-days cadence, wider-field ULTRASAT survey(s) can be used for BLR RM, maximizing the pool of potential targets. Smaller samples of low-luminosity (low-mass) sources can be better studied within the nearly continuous ULTRASAT fields. The variability-selected AGNs should then be dynamically targeted with ground-based spectroscopy and/or narrow-/medium-band imaging (see above). Tailoring the narrow/medium bands for each target will allow one to decompose and measure line and continuum emission, per epoch. Spectroscopy for bright enough targets may facilitate velocity-resolved RM, and shed light on the BLR structure and kinematics.

Continuum and accretion disk reverberation mapping. Recent RM and microlensing studies suggest that accretion disks in quasars are a factor of a few larger than predicted by simple thin disk models (e.g., Blackburne et al. 2011; Fausnaugh et al. 2016), with potential implications for understanding accretion in general, and SMBH fueling in particular. However, some of those findings have been recently challenged by high-fidelity continuum RM campaigns, which suggest nonnegligible continuum emission from the BLR in quasars may be contaminating the longer-lag RM signal (e.g., Chelouche et al. 2019; Netzer 2022). This generally overlooked BLR emission component could alleviate the tension between disk theory and observations, and also provide a novel window into BLR physics. High-cadence and precise UV monitoring is crucial for disk (and continuum) RM studies, since this inner disk (seed) emission allows one to anchor the entire observed lag–wavelength relation (see, e.g., Figure 5 in Fausnaugh et al. 2016). Such UV monitoring is obviously very challenging to pursue with existing facilities, even for single targets.

ULTRASAT will allow us to measure disk and diffuse (BLR-driven) continuum lags in a sizeable sample of $z \lesssim 0.5$ AGNs. In this case, the typical thin disk sizes $\sim$ 1–5 lt-days mean that targets will be selected from the nearly continuous, staring-mode ULTRASAT field(s). As for the simultaneous optical follow-up observations, the narrow-/medium-band imaging should include several line-free spectral regions (but see below for an alternative approach). Adding a few line-focused bands would enable broad-line RM to be done in parallel.

Single-band reverberation mapping. Several studies have suggested that it is possible to measure BLR reverberation timescales using single-band observations (Zu et al. 2016; Springer & Ofek 2021a, 2021b). Generally, the idea is that the observed quasar variability distribution would be comprised of a dominant driving signal (i.e., a power law or damped-random-walk-shaped PSD or SF; see above) and a superimposed (weak) reverberating signal.

The recent work by Springer & Ofek (2021a, 2021b) suggests that identifying this latter reverberating signal may be possible if the emission line is sufficiently strong, i.e., if the equivalent width is $\gtrsim$10% of the observed band. For $z \sim 1$ quasars, the Lyα line shifted to the ULTRASAT band and its equivalent width may be of the order of 30% of the band. This novel method requires a large number of targets and a high cadence, which ULTRASAT may provide in its nearly continuous, staring-mode fields if we maximize the number of accessible AGNs in them. Alternatively, this method may be best applied for a future wider-area and somewhat slower cadence ULTRASAT survey (i.e., a possible medium tier survey).

We expect that ULTRASAT's main advantage would arise by comparing the (effective) time delays of large subsets of quasars in given redshift intervals. This would allow us to understand better the scatter in the relations linking BLR size and AGN luminosity, where this scatter is influenced by additional AGN properties, such as the mass accretion rate (expanding on pioneering studies of small samples; see, e.g., Du et al. 2018 and references therein).

5.8.3. Extreme Active Galactic Nucleus Variability and Supermassive Black Hole–related Transients

Time-domain surveys have recently started to reveal new types of extreme variability and of transient phenomena associated with accretion onto SMBHs. Observationally, these include (1) persistent AGNs that vary by more than ≈1 mag on timescales of a few years (or less; e.g., Lawrence et al. 2016; Rumbaugh et al. 2018); (2) "changing look" AGN—systems where the blue continuum and/or broad-line emission typical of (unobscured) AGNs (dis-)appears (e.g., LaMassa et al. 2015; Runnoe et al. 2016; MacLeod et al. 2019; Green et al. 2022), sometimes on timescales of weeks to months (e.g., Gezari et al. 2017; Trakhtenbrot et al. 2019a; Zeltyn et al. 2022); (3) a growing number of nuclear transients in previously known AGNs, exhibiting peculiar properties in their light curves, spectra, and/or multiwavelength SEDs (e.g., Drake et al. 2011; Blanchard et al. 2017; Kankare et al. 2017; Trakhtenbrot et al. 2019b; Frederick et al. 2021); and (4) other nuclear transients, in previously inactive nuclei, which exhibit some AGN-like features (along with some non-AGN features), and which may be driven by relevant processes (e.g., Neustadt et al. 2020; Malyali et al. 2021; Homan et al. 2023). These phenomena challenge decades-old models for SMBH accretion flows (Lawrence 2018), and provide an unprecedented opportunity to explore accretion physics and SMBH fueling.

Most AGN-related transients are characterized by blue continuum emission, strongly rising toward the UV, and hints for intense ionizing radiation (based on certain spectral features). In many cases the UV flares are much more pronounced than the optical ones. These events are rare, comparable to (and perhaps rarer than) TDEs (Section 5.7). Practically, we are currently identifying roughly one transient of interest per month, based solely on public alerts based on optical imaging. A sufficiently wide NUV survey (thousands of square degrees) with few-days cadence could yield hundreds of events per year.

ULTRASAT will allow us to detect and survey AGN- and SMBH-related transients in the regime which most closely probes the inner workings of the accretion flows. The nearly real-time data analysis will allow us to trigger key follow-up multiwavelength observations (practically focusing on $z \lesssim 1$), and to probe the light-curve peak, which is often missed in current efforts. AGN transients of particular interest include (1) events that combine a sharp rise followed by a plateau near the Eddington luminosity—thus probing super-Eddington accretion, and (2) flaring AGNs driven by TDEs that perturb preexisting thin accretion disks (e.g., Merloni et al. 2015; Chan et al. 2019). The well-designed nature of the ULTRASAT survey(s) will allow us to determine the occurrence rates of various (classes of) AGN-related transients, which is important to understand their driving mechanisms and role in SMBH growth.

5.8.4. Strongly Lensed Quasars

Identifying strongly lensed quasars enables studies of dark matter halos (e.g., Maoz & Rix 1993), galaxy evolution (e.g., Ofek et al. 2003), interiors (Kochanek 2004), and cosmography (e.g., Treu & Marshall 2016; but see also Blum et al. 2020; Kochanek 2020). While the low spatial resolution of ULTRASAT is insufficient to resolve the multiple images of strongly lensed quasars, the high-cadence ULTRASAT light curves will allow us to identify such systems based on the combined variability of their flux and center of light (following Springer & Ofek 2021a, 2021b).

5.8.5. Other Active Galactic Nucleus–related Science

We briefly mention a few other AGN-related science projects enabled by ULTRASAT data.

Identifying active galactic nucleus signatures in compact radio sources. These signatures can be used to test models of jet launching and AGN reignition (e.g., Mooley et al. 2016).

Studying the spectral energy distributions of jetted active galactic nuclei (blazars). These SEDs can be used to distinguish between disk- and jet-dominated emission mechanisms (e.g., Rodrigues et al. 2021).

Selecting "background" quasars, based on variability. These will enable studies of galaxies and their circumgalactic medium (Tumlinson et al. 2017). ULTRASAT will greatly expand on previous similar efforts (e.g., with GALEX; see Wasleske et al. 2022).

5.9. Galaxies

ULTRASAT will produce the most sensitive all-sky NUV galaxy survey yet. Moreover, the combined depth achieved in its high-cadence field(s) will yield sensitivities greatly exceeding the deepest GALEX fields, and competitive with medium deep HST UV observations, albeit limited by crowding in the faintest fluxes.

We base our galaxy count estimates on the point-source sensitivity shown in Figure 6, since a majority of galaxies near the ULTRASAT detection threshold will be compact compared to the PSF. We adopt a NUV number–magnitude relation based on a combination of GALEX NUV data (Xu et al. 2005), Neil Gehrels Swift Satellite (Swift) UVOT uvw1 data (Hoversten et al. 2009), and HST F275W data (Teplitz et al. 2013). Both the Swift and HST data are well matched in central wavelength to the ULTRASAT band, while the GALEX NUV channel is slightly bluer. Together, these sources provide estimates of the surface density for $15 \lesssim m_{\rm AB} \lesssim 27$.

Combining these number–flux relations with the survey modes outlined in Section 3.1, we have estimated the total galaxy samples expected in the ULTRASAT data. The result is plotted in Figure 13. In total, we anticipate that ULTRASAT will detect (at $\geqslant 5\sigma$) a sample $\sim 3 \times 10^8$ galaxies, dominated by the high-latitude sky $|b| > 30^\circ$ where the deeper portion of the all-sky survey will typically achieve magnitude limits near $m_{\rm AB} = 24$.

Because the total ULTRASAT exposures in the time-domain fields may exceed 10^4 hr, crowding is a critical consideration. We have calculated the crowding limit expected by applying the analytical treatment from Condon (1974), using a power law fit to the number–flux relation from Hoversten et al. (2009). Because the PSF FWHM varies substantially with field angle for ULTRASAT, we kept the FWHM as a free parameter. The resulting limits are shown in Figure 14. We have neglected the stellar contribution to the confusion noise. This is justified at high Galactic latitudes b because galaxy counts exceed star counts for $m_{\rm AB} \gtrsim 21$ for $|b| \gtrsim 30^\circ$ (Xu et al. 2005). (Near the plane of the Galaxy, a more thorough treatment that includes confusion by Galactic stars would be appropriate.)

It will be possible to measure the NUV fluxes of objects somewhat fainter than the nominal crowding limit in cases

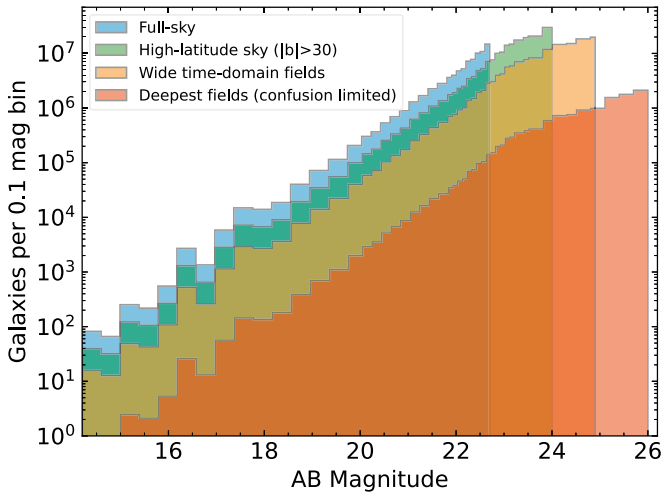

Figure 13. Expected number–magnitude distribution for galaxies in the ULTRASAT surveys. Different colors represent different tiers of the ULTRASAT surveys. The all-sky survey is subdivided into the high-latitude portion (green) and the shallower observations over the full sky including low Galactic latitudes (blue). The time-domain fields are similarly divided into the low-cadence, wide area portion (yellow) and the deepest fields (red). Each colored histogram is cut off at the magnitude limit appropriate to that survey's anticipated integration time and the 10″–11″ PSF expected over most of the field, except for the deep field histogram, which terminates at the 5σ confusion limit for a 6″ PSF. See text for a discussion of the samples upon which the plot is based.

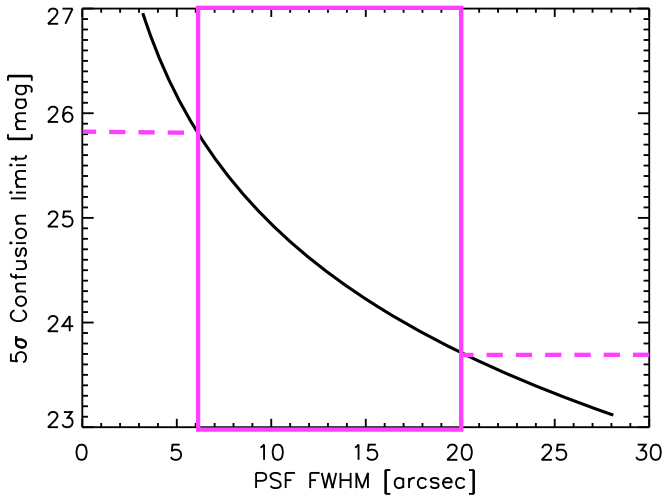

Figure 14. The 5σ confusion limit for NUV imaging is plotted as a function of PSF size. The key range for ULTRASAT is approximately $6'' \leqslant \mathrm{FWHM} \lesssim 20''$ (see Figure 5). Within its annulus of best focus ($4^\circ < \theta < 6^\circ$ off axis), ULTRASAT can be used to study galaxies as faint as $m_{\mathrm{AB}} \approx 26$ with integration times ~ 50 hr.

where good priors can be derived from higher-resolution imaging at other wavelengths. Such approaches have been applied in past analyses of Spitzer Space Telescope data, and are under active consideration for the analysis of Rubin data in combination with higher-resolution data from Euclid or the Nancy Grace Roman Space Telescope.

As an example of ULTRASAT's impact on galaxy surveys, we estimate the benefit of having sensitive NUV data when computing photometric redshifts. The accuracy of photometric reshifts can be greatly improved by sampling wavelengths that span prominent spectral features like the Lyman break at 912 Å. ULTRASAT's bandpass covering 230–290 nm will be used to confirm this spectral break in $z \sim 2$ galaxies.

To quantify our ability to recover photometric redshifts with ULTRASAT, we take the COSMOS2020 catalog (Weaver et al. 2022) and degrade the *ugrizy* flux errors to the 5 yr Rubin depths (*ugrizy* = 25.7, 27.0, 27.1, 26.4, 25.7, and 24.5 (5σ), respectively), which will be available over 18,000 deg^2 by the end of ULTRASAT's prime mission. The COSMOS2020 catalog also contains GALEX NUV data with a 3σ depth of 26 AB mag, comparable to the deepest ULTRASAT fields. We produce two *ugrizy* catalogs, one with NUV data and one without, to simulate a survey with and without ULTRASAT. We use the code EAZY (Brammer et al. 2008) to obtain photometric redshifts and compare our results to known spectroscopic redshifts from the SDSS, zCOSMOS, and DEEP3 surveys (Lilly et al. 2009; Cooper et al. 2012; Ahumada et al. 2020). These spectroscopic redshifts range from $z = 0$ to 3.5 with an average of $z = 0.5$. We find that including the NUV photometry primarily improves the fraction of catastrophic photo-z failures ($\Delta(z)/(1+z) > 0.15$), which drops from 25% with optical data alone to 17% with the inclusion of the NUV band, over the full redshift range tested (which is dominated by galaxies at $0 < z < 2$).

We anticipate a stronger impact on the false-positive rate for Lyman-break galaxies (LBGs) at $2.2 < z < 2.8$, where the Lyman break results in no flux in the ULTRASAT NUV band, while all optical passbands accessible to ground-based telescopes will show strong detections for blue, actively star-forming galaxies. At this redshift, the characteristic 1500 Å magnitude $M^* = -20.97$ (Bouwens et al. 2015), corresponding to $m^*_{\mathrm{AB}} \approx 24.3$. The deepest ULTRASAT photometry will go 2 mag deeper than this, and combined with Rubin data will yield complete samples of LBGs down to M^* for hundreds or thousands of square degrees.

5.10. Solar System

ULTRASAT's all-sky UV map observations will be sufficient to measure the NUV color of more than 10^4 asteroids, at different sections of the main belt of asteroids. Studies examining the NUV range of minerals and meteorites show that the NUV spectral region is sensitive to different mineral properties, thus it might provide complementary capabilities and opportunities for asteroid classification (e.g., Hendrix & Vilas 2006; Cloutis et al. 2008). Color differences between the main asteroid types (S-type—silicate-based minerals; C-type—carbonaceous-based minerals) were measured by the GALEX space telescope (Waszczak et al. 2015) and the IUE (Roettger & Buratti 1994).

Since the NUV region is a sensitive indicator of the presence of even trace amounts (<0.01 wt%) of ferrum (Cloutis et al. 2008), it has the potential to break the degeneracy in both the visible and NIR ranges (DeMeo et al. 2009) between the spectral signature of metal asteroids (M type) and primitive/organic asteroids (P type). NUV measurements from GALEX show a mean difference of about 0.3 mag between these two types (Figure 15). This difference is well above the photometric uncertainty of ULTRASAT, estimated as 1%. This difference can also be seen on the surface of the large asteroid 1 Ceres (which belongs to the C-type classification), which was found to present a deep absorption band at around 250 nm (Li et al. 2008), while metal meteorites have a fixed slope in the NUV range with no light diminution (Cloutis et al. 2008).

Both M-type and P-type asteroids are defined by flat, almost feature-less, reflectance spectra (Figure 16) that usually hide

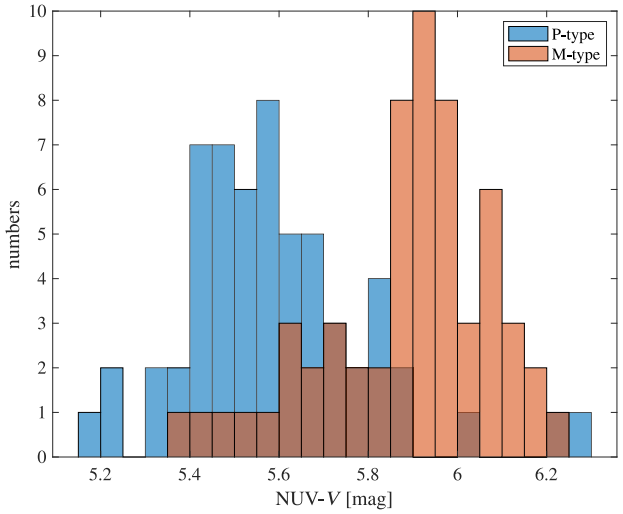

Figure 15. Distribution of NUV − V colors of P- (bluish) and M-type (reddish) asteroids measured by the GALEX space telescope (Waszczak et al. 2015). The V magnitudes are from the Minor Planet Center. Mean values are separated by about 0.3 mag, a value which is larger value than the ULTRASAT photometric precision.

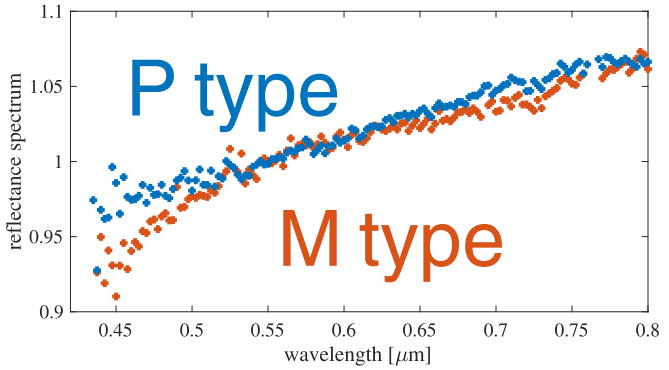

Figure 16. Visible reflectance spectra of asteroids 125 Liberatrix (M type, reddish) and 46 Hestia (P type, bluish). The data are from the SMASS library (http://smass.mit.edu/), while the observations and classifications were conducted by Bus & Binzel (2002).

well within the error range of measured spectra. They are only distinguished from one another when an albedo value is available, with P types having low values and M types have mid-range values. However, a secure albedo value with low uncertainty is hardly available, which prevents their correct identification, and makes the ULTRASAT measurements valuable for asteroid studies.

Disentangling between the M types and the P types might solve the "missing mantle problem" (Burbine et al. 1996)—the inconsistency between the numbers of M types that supposedly originate from the inner cores of differentiated planetesimals later destroyed by catastrophic collisions, to the number of asteroids originated from the mantle layers of the same destroyed differentiated planetesimals (dubbed as A-type asteroids). A possible answer lays within a wrong identification of P-type asteroids and defining them as M-type asteroids, due to their reflectance spectra resemblance in both the visible and NIR ranges. Therefore, ULTRASAT NUV colors of asteroids have the potential to solve this inconsistency, resulting in fine-tuned models of planetesimal formation.

6. Summary

We have described ULTRASAT, a wide-field time-domain UV space telescope that is expected to be launched in 2027 (see Table 1 for ULTRASAT's key properties). ULTRASAT's design (Section 2) and operation modes (Section 3) are optimized for studying the transient and variable UV sky. With a grasp (i.e., instantaneous volume of the Universe accessible for transient searches) much larger than that of current surveys and comparable to that of the planned Rubin/LSST (see Figure 1), ULTRASAT will be at the forefront of time-domain astronomy both as a transient discovery machine driving vigorous ground- and space-based follow-up campaigns, as well as an optimal and fast-response follow-up facility. ULTARSAT's location at GEO will enable it to distribute transient alerts publicly within 15 minutes from imaging, and its agility will enable it to access any point in the observable sky (>50% of the sky at any time) within 15 minutes from an external transient alert received at the SOC (Section 4).

The large enhancement of the discovery rate of transients and the continuous minute to month cadence UV light curves that will be provided by ULTRASAT, will have a significant impact on a wide range of astrophysics research areas (see Table 2 and Section 5), ranging from high-energy extragalactic sources such as BNS and NS–BH mergers, SNe, TDEs, AGNs, and GRBs, through to active and flaring stars and exoplanet host stars, up to solar system objects.

The key science goals, which defined the required technical capabilities of ULTRASAT, are the discovery and observation of EM emission from BNS mergers and SNe.

1. With a large fraction (>50%) of the sky instantaneously accessible, fast (minutes) slewing capability, and a FOV that covers the error ellipses expected from GW detectors beyond 2026 for events at distances of $\lesssim$300 Mpc, ULTRASAT is expected to be the best observatory for detecting EM counterparts of GW events produced by mergers involving NSs (see Figure 2, Section 5.1). Measuring the EM emission following BNS/NS–BH mergers will (i) provide direct constraints on the structure and composition of the ejected material, thus providing unique diagnostics of the properties of matter at nuclear density and of the merger dynamics, (ii) enable us to determine whether mergers are the sources of r-process elements and GRBs, and (iii) allow us to determine the location in, and properties of, the host galaxy, thus revealing the stellar antecedents of the binary systems. The early UV light curves will provide unique constraints and will be highly useful for discriminating between different models of the structure and composition of the ejecta (Section 5.1.3).
2. ULTRASAT will detect hundreds of SNe within the first day from explosion, and tens within the first hour—a discovery rate which is an order of magnitude larger than that of any other survey (see Figure 2, Section 5.2). This will allow us, for the first time, to detect shock breakouts systematically and to construct early (<1 day) continuous high-cadence (minutes) UV light curves for hundreds of core-collapse SNe, including for rarer BSG and W-R SN progenitor types. Measuring this early shock breakout/cooling part of SN light curves will provide unique information of the progenitor stars and their preexplosion evolution, in particular mapping the different types of SNe to the different

stellar progenitors, and hence also constraints on the explosion mechanisms, which are not fully understood.

Acknowledgments

E.W.'s research is partially supported by ISF, GIF, and IMOS grants. A.G.Y.'s research is supported by the EU via ERC grant No. 725161, the ISF GW Excellence Center, an IMOS space infrastructure grant, and a GIF grant, as well as the André Deloro Institute for Advanced Research in Space and Optics, The Helen Kimmel Center for Planetary Science, the Schwartz/Reisman Collaborative Science Program, and the Norman E Alexander Family M Foundation ULTRASAT Data Center Fund, Minerva, and Yeda-Sela. A.G.Y. is the incumbent of the The Arlyn Imberman Professorial Chair. E.O.O. is grateful for the support of grants from the Willner Family Leadership Institute, André Deloro Institute, Paul and Tina Gardner, The Norman E Alexander Family M Foundation ULTRASAT Data Center Fund, Israel Science Foundation, Israeli Ministry of Science, Minerva, BSF, BSF-transformative, NSF-BSF, Israel Council for Higher Education (VATAT), Sagol Weizmann-MIT, Yeda-Sela, and Weizmann-UK. S.B.A. is grateful for support from the Willner family foundation, Israel Science Foundation, Israel Ministry of Science, Minerva, and the Azrieli Foundation. N.C.S. is supported by the Israel Science Foundation (Individual Research grant 2565/19) and the Binational Science foundation (grant Nos. 2019772 and 2020397). B.T. acknowledges support from the European Research Council (ERC) under the European Union's Horizon 2020 research and innovation program (grant agreement 950533) and from the Israel Science Foundation (grant 1849/19). I.A. is a CIFAR Azrieli Global Scholar in the Gravity and the Extreme Universe Program and acknowledges support from that program, from the European Research Council (ERC) under the European Union's Horizon 2020 research and innovation program (grant agreement number 852097), from the Israel Science Foundation (grant No. 2752/19), from the United States—Israel Binational Science Foundation (BSF), and from the Israeli Council for Higher Education Alon Fellowship.

ORCID iDs

Y. Shvartzvald https://orcid.org/0000-0003-1525-5041
A. Gal-Yam https://orcid.org/0000-0002-3653-5598
I. Arcavi https://orcid.org/0000-0001-7090-4898
B. Trakhtenbrot https://orcid.org/0000-0002-3683-7297
I. Wold https://orcid.org/0000-0002-0784-1852

References

Abbott, B. P., Abbott, R., Abbott, T. D., et al. 2016a, PhRvL, 116, 061102
Abbott, B. P., Abbott, R., Abbott, T. D., et al. 2016b, LRR, 19, 1
Abbott, B. P., Abbott, R., Abbott, T. D., et al. 2017a, PhRvL, 119, 161101
Abbott, B. P., Abbott, R., Abbott, T. D., et al. 2017b, Natur, 551, 85
Abbott, B. P., Abbott, R., Abbott, T. D., et al. 2018, LRR, 21, 3
Abbott, B. P., Abbott, R., Abbott, T. D., et al. 2020, LRR, 23, 3
Abbott, B. P., Abbott, R., Abbott, T. D., et al. 2017c, Natur, 551, 85
Afsariardchi, N., & Matzner, C. D. 2018, ApJ, 856, 146
Agol, E. 2011, ApJL, 731, L31
Ahumada, R., Allende Prieto, C., Almeida, A., et al. 2020, ApJS, 249, 3
Amanullah, R., Johansson, J., Goobar, A., et al. 2015, MNRAS, 453, 3300
Andrews, J. E., Sand, D. J., Valenti, S., et al. 2019, ApJ, 885, 43
Angel, J. R. P., Borra, E. F., & Landstreet, J. D. 1981, ApJS, 45, 457
Anglada-Escudé, G., Amado, P. J., Barnes, J., et al. 2016, Natur, 536, 437
Arcavi, I. 2018, ApJL, 855, L23
Arcavi, I., Gal-Yam, A., Sullivan, M., et al. 2014, ApJ, 793, 38
Arévalo, P., & Uttley, P. 2006, MNRAS, 367, 801
Asif, A., Barschke, M., Bastian-Querner, B., et al. 2021, Proc. SPIE, 11821, 118210U
Astudillo-Defru, N., Delfosse, X., Bonfils, X., et al. 2017, A&A, 600, A13
Balberg, S., & Loeb, A. 2011, MNRAS, 414, 1715
Banerjee, S., Tanaka, M., Kato, D., et al. 2022, ApJ, 934, 117
Banerjee, S., Tanaka, M., Kawaguchi, K., Kato, D., & Gaigalas, G. 2020, ApJ, 901, 29
Barack, L., Cardoso, V., Nissanke, S., et al. 2019, CQGra, 36, 143001
Bastian-Querner, B., Kaipachery, N., Küster, D., et al. 2021, Proc. SPIE, 11819, 118190F
Bellm, E. C., Kulkarni, S. R., Graham, M. J., et al. 2019, PASP, 131, 018002
Ben-Ami, S., Ofek, E. O., Polishook, D., et al. 2023, PASP, 135, 085002
Ben-Ami, S., Shvartzvald, Y., Waxman, E., et al. 2022, Proc. SPIE, 12181, 1218105
Bentz, M. C., Denney, K. D., Grier, C. J., et al. 2013, ApJ, 767, 149
Bentz, M. C., & Katz, S. 2015, PASP, 127, 67
Berger, E., Kulkarni, S. R., Frail, D. A., & Soderberg, A. M. 2003, ApJ, 599, 408
Betoule, M., Kessler, R., Guy, J., et al. 2014, A&A, 568, A22
Bianco, F. B., Howell, D. A., Sullivan, M., et al. 2011, ApJ, 741, 20
Blackburne, J. A., Pooley, D., Rappaport, S., & Schechter, P. L. 2011, ApJ, 729, 34
Blanchard, P. K., Nicholl, M., Berger, E., et al. 2017, ApJ, 843, 106
Bloemen, S., Groot, P., Nelemans, G., & Klein-Wolt, M. 2015, in ASP Conf. Ser. 496, Living Together: Planets, Host Stars and Binaries, ed. S. M. Rucinski, G. Torres, & M. Zejda (San Francisco, CA: ASP), 254
Bloom, J. S., Giannios, D., Metzger, B. D., et al. 2011, Sci, 333, 203
Blum, K., Castorina, E., & Simonović, M. 2020, ApJL, 892, L27
Boehner, P., Plewa, T., & Langer, N. 2017, MNRAS, 465, 2060
Bonnerot, C., & Stone, N. C. 2021, SSRv, 217, 16
Bouwens, R. J., Illingworth, G. D., Oesch, P. A., et al. 2015, ApJ, 803, 34
Brammer, G. B., van Dokkum, P. G., & Coppi, P. 2008, ApJ, 686, 1503
Bricman, K., & Gomboc, A. 2020, ApJ, 890, 73
Briegal, J. T., Gillen, E., Queloz, D., et al. 2022, MNRAS, 513, 420
Brout, D., Scolnic, D., Kessler, R., et al. 2019, ApJ, 874, 150
Brown, P. J., Perry, J. M., Beeny, B. A., Milne, P. A., & Wang, X. 2018, ApJ, 867, 56
Buccino, A. P., Lemarchand, G. A., & Mauas, P. J. D. 2006, Icar, 183, 491
Budnik, R., Katz, B., Sagiv, A., & Waxman, E. 2010, ApJ, 725, 63
Bulla, M. 2023, MNRAS, 520, 2558
Bulla, M., Coughlin, M. W., Dhawan, S., & Dietrich, T. 2022, Univ, 8, 289
Burbine, T. H., Meibom, A., & Binzel, R. P. 1996, M&PS, 31, 607
Burke, J., Howell, D. A., Sand, D. J., et al. 2022, arXiv:2207.07681
Burrows, A., & Vartanyan, D. 2021, Natur, 589, 29
Bus, S. J., & Binzel, R. P. 2002, Icar, 158, 146
Cackett, E. M., Bentz, M. C., & Kara, E. 2021, iSci, 24, 102557
Calzavara, A. J., & Matzner, C. D. 2004, MNRAS, 351, 694
Campana, S., Mangano, V., Blustin, A. J., et al. 2006, Natur, 442, 1008
Canto Martins, B. L., Gomes, R. L., Messias, Y. S., et al. 2020, ApJS, 250, 20
Cao, Y., Kulkarni, S. R., Howell, D. A., et al. 2015, Natur, 521, 328
Caplar, N., Lilly, S. J., & Trakhtenbrot, B. 2017, ApJ, 834, 111
Cardelli, J. A., Clayton, G. C., & Mathis, J. S. 1989, ApJ, 345, 245
Cassan, A., Kubas, D., Beaulieu, J.-P., et al. 2012, Natur, 481, 167
Chambers, K. C., Magnier, E. A., Metcalfe, N., et al. 2016, arXiv:1612.05560
Chan, C.-H., Piran, T., Krolik, J. H., & Saban, D. 2019, ApJ, 881, 113
Chelouche, D., Pozo Nuñez, F., & Kaspi, S. 2019, NatAs, 3, 251
Chelouche, D., Shemmer, O., Cotlier, G. I., Barth, A. J., & Rafter, S. E. 2014, ApJ, 785, 140
Chelouche, D., & Zucker, S. 2013, ApJ, 769, 124
Chevalier, R. A. 2012, ApJL, 752, L2
Chevalier, R. A., & Irwin, C. M. 2011, ApJL, 729, L6
Chornock, R., Berger, E., Gezari, S., et al. 2014, ApJ, 780, 44
Christian, D. J., Craig, N., Cahill, W., Roberts, B., & Malina, R. F. 1999, AJ, 117, 2466
Cloutis, E. A., McCormack, K. A., Bell, J. F., et al. 2008, Icar, 197, 321
Combi, L., & Siegel, D. 2023, ApJ, 944, 28
Condon, J. J. 1974, ApJ, 188, 279
Cooper, M. C., Griffith, R. L., Newman, J. A., et al. 2012, MNRAS, 419, 3018
Cowan, J. J., Sneden, C., Lawler, J. E., et al. 2021, RvMP, 93, 015002
Cowperthwaite, P. S., Berger, E., Villar, V. A., et al. 2017, ApJL, 848, L17
Crosley, M. K., & Osten, R. A. 2018, ApJ, 862, 113
Davenport, J. R. A., & Covey, K. R. 2018, ApJ, 868, 151
Dean, C., Fernández, R., & Metzger, B. D. 2021, ApJ, 921, 161
Debes, J. H., & Sigurdsson, S. 2002, ApJ, 572, 556

DeMeo, F. E., Binzel, R. P., Slivan, S. M., & Bus, S. J. 2009, Icar, 202, 160
Dilday, B., et al. 2010, ApJ, 713, 1026
Dimitriadis, G., Maguire, K., Karambelkar, V. R., et al. 2023, MNRAS, 521, 1162
Domoto, N., Tanaka, M., Kato, D., et al. 2022, ApJ, 939, 8
Dorsman, B., Raaijmakers, G., Cenko, S. B., et al. 2023, ApJ, 944, 126
Drake, A. J., Djorgovski, S. G., Mahabal, A., et al. 2011, ApJ, 735, 106
Drout, M. R., Piro, A. L., Shappee, B. J., et al. 2017, Sci, 358, 1570
Du, P., Zhang, Z.-X., Wang, K., et al. 2018, ApJ, 856, 6
Dupuis, J., Chayer, P., Vennes, S., Christian, D. J., & Kruk, J. W. 2000, ApJ, 537, 977
Fakhouri, H. K., Boone, K., Aldering, G., et al. 2015, ApJ, 815, 58
Fausnaugh, M. M., Denney, K. D., Barth, A. J., et al. 2016, ApJ, 821, 56
Fausnaugh, M. M., Vallely, P. J., Kochanek, C. S., et al. 2021, ApJ, 908, 51
Feindt, U., Nordin, J., Rigault, M., et al. 2019, JCAP, 2019, 005
Fernández, R., & Metzger, B. D. 2016, ARNPS, 66, 23
Fleming, B. T., France, K., Nell, N., et al. 2018, JATIS, 4, 014004
Foley, R. J., Smith, N., Ganeshalingam, M., et al. 2007, ApJL, 657, L105
Fossati, L., Bagnulo, S., Elmasli, A., et al. 2010, ApJ, 720, 872
France, K., Froning, C. S., Linsky, J. L., et al. 2013, ApJ, 763, 149
France, K., Loyd, R. O. P., Youngblood, A., et al. 2016, ApJ, 820, 89
Frank, J., & Rees, M. J. 1976, MNRAS, 176, 633
Frederick, S., Gezari, S., Graham, M. J., et al. 2021, ApJ, 920, 56
Fremling, C., Miller, A. A., Sharma, Y., et al. 2020, ApJ, 895, 32
Fryer, C. L., Fontes, C. J., Warsa, J. S., et al. 2020, ApJ, 898, 123
Fujibayashi, S., Kiuchi, K., Nishimura, N., Sekiguchi, Y., & Shibata, M. 2018, ApJ, 860, 64
Fuller, J., & Ro, S. 2018, MNRAS, 476, 1853
Fulton, B. J., Tonry, J. L., Flewelling, H., et al. 2014, ApJ, 796, 114
Gaia Collaboration, Brown, A. G. A., Vallenari, A., et al. 2018, A&A, 616, A1
Gaia Collaboration, Brown, A. G. A., Vallenari, A., et al. 2021, A&A, 649, A1
Ganot, N., Gal-Yam, A., Ofek, E. O., et al. 2016, ApJ, 820, 57
Ganot, N., Ofek, E. O., Gal-Yam, A., et al. 2022, ApJ, 931, 71
Gänsicke, B. T., Koester, D., Farihi, J., et al. 2012, MNRAS, 424, 333
Gezari, S. 2021, ARA&A, 59, 21
Gezari, S., Basa, S., Martin, D. C., et al. 2008a, ApJ, 676, 944
Gezari, S., Chornock, R., Rest, A., et al. 2012, Natur, 485, 217
Gezari, S., Dessart, L., Basa, S., et al. 2008b, ApJL, 683, L131
Gezari, S., Hung, T., Cenko, S. B., et al. 2017, ApJ, 835, 144
Gezari, S., Jones, D. O., Sanders, N. E., et al. 2015, ApJ, 804, 28
Gillanders, J. H., Smartt, S. J., Sim, S. A., Bauswein, A., & Goriely, S. 2022, MNRAS, 515, 631
Ginet, G. P., O'Brien, T. P., Huston, S. L., et al. 2013, SSRv, 179, 579
Ginzburg, S., & Balberg, S. 2012, ApJ, 757, 178
Goldberg, J. A., Jiang, Y.-F., & Bildsten, L. 2022, ApJ, 933, 164
Goldstein, D. A., Nugent, P. E., Kasen, D. N., & Collett, T. E. 2018, ApJ, 855, 22
Goobar, A., Amanullah, R., Kulkarni, S. R., et al. 2017, Sci, 356, 291
Goobar, A., & Leibundgut, B. 2011, ARNPS, 61, 251
Gorbovskoy, E. S., Lipunov, V. M., Kornilov, V. G., et al. 2013, ARep, 57, 233
Gordon, T. A., Davenport, J. R. A., Angus, R., et al. 2021, ApJ, 913, 70
Gottlieb, O., Nakar, E., & Piran, T. 2018, MNRAS, 473, 576
Goyal, J. M., Mayne, N., Sing, D. K., et al. 2018, MNRAS, 474, 5158
Granot, J., De Colle, F., & Ramirez-Ruiz, E. 2018, MNRAS, 481, 2711
Green, P. J., Pulgarin-Duque, L., Anderson, S. F., et al. 2022, ApJ, 933, 180
Greene, J. E., Strader, J., & Ho, L. C. 2020, ARA&A, 58, 257
Guillochon, J., & Ramirez-Ruiz, E. 2015, ApJ, 809, 166
Guy, J., Astier, P., Baumont, S., et al. 2007, A&A, 466, 11
Hallakoun, N., Maoz, D., Agol, E., et al. 2018, MNRAS, 476, 933
Hallakoun, N., Xu, S., Maoz, D., et al. 2017, MNRAS, 469, 3213
Hamidani, H., & Ioka, K. 2023, MNRAS, 524, 4841
Heinze, A. N., Tonry, J. L., Denneau, L., et al. 2018, AJ, 156, 241
Hendrix, A. R., & Vilas, F. 2006, AJ, 132, 1396
Hills, J. G. 1975, Natur, 254, 295
Hiramatsu, D., Tsuna, D., Berger, E., et al. 2023, ApJL, 955, L8
Ho, A. Y. Q., Perley, D. A., Yao, Y., et al. 2022, ApJ, 938, 85
Homan, D., Krumpe, M., Markowitz, A., et al. 2023, A&A, 672, A167
Homayouni, Y., Trump, J. R., Grier, C. J., et al. 2020, ApJ, 901, 55
Hosseinzadeh, G., Sand, D. J., Valenti, S., et al. 2017, ApJL, 845, L11
Hotokezaka, K., Tanaka, M., Kato, D., & Gaigalas, G. 2021, MNRAS, 506, 5863
Hotokezaka, K., Tanaka, M., Kato, D., & Gaigalas, G. 2022, MNRAS, 515, L89
Hoversten, E. A., Gronwall, C., Berk, D. E. V., et al. 2009, ApJ, 705, 1462
Hung, T., Gezari, S., Blagorodnova, N., et al. 2017, ApJ, 842, 29
Hung, T., Gezari, S., Jones, D. O., et al. 2016, ApJ, 833, 226
Husser, T. O., Wende-von Berg, S., Dreizler, S., et al. 2013, A&A, 553, A6
Irani, I., Chen, P., Morag, J., et al. 2024, ApJ, 962, 109
Irani, I., Morag, J., Gal-Yam, A., et al. 2023, arXiv:2310.16885
Ivezić, Ž, Kahn, S. M., Tyson, J. A., et al. 2019, ApJ, 873, 111
Jacobson-Galán, W. V., Dessart, L., Jones, D. O., et al. 2022, ApJ, 924, 15
Jacobson-Galán, W. V., Dessart, L., Margutti, R., et al. 2023, ApJL, 954, L42
Janka, H.-T., Melson, T., & Summa, A. 2016, ARNPS, 66, 341
Jiang, J.-A., Doi, M., Maeda, K., et al. 2017, Natur, 550, 80
Jonker, P. G., Stone, N. C., Generozov, A., van Velzen, S., & Metzger, B. 2020, ApJ, 889, 166
Jura, M. 2003, ApJL, 584, L91
Kankare, E., Kotak, R., Mattila, S., et al. 2017, NatAs, 1, 865
Kara, E., Alston, W. N., Fabian, A. C., et al. 2016, MNRAS, 462, 511
Kasen, D. 2010, ApJ, 708, 1025
Kasen, D., Metzger, B., Barnes, J., Quataert, E., & Ramirez-Ruiz, E. 2017, Natur, 551, 80
Kasliwal, M. M., Nakar, E., Singer, L. P., et al. 2017, Sci, 358, 1559
Kaspi, S., Smith, P. S., Netzer, H., et al. 2000, ApJ, 533, 631
Katz, B., Budnik, R., & Waxman, E. 2010, ApJ, 716, 781
Katz, B., Sapir, N., & Waxman, E. 2012, ApJ, 747, 147
Kelly, B. C., Treu, T., Malkan, M., Pancoast, A., & Woo, J.-H. 2013, ApJ, 779, 187
Kenworthy, W. D., et al. 2021, ApJ, 923, 265
Khabibullin, I., & Sazonov, S. 2014, MNRAS, 444, 1041
Kim, A., Aldering, G., Antilogus, P., et al. 2019a, BAAS, 51, 140
Kim, J., Im, M., Choi, C., & Hwang, S. 2019b, ApJ, 884, 103
Kim, S.-L., Lee, C.-U., Park, B.-G., et al. 2016, JKAS, 49, 37
Kochanek, C. S. 2004, ApJ, 605, 58
Kochanek, C. S. 2016, MNRAS, 461, 371
Kochanek, C. S. 2020, MNRAS, 493, 1725
Koester, D., Gänsicke, B. T., & Farihi, J. 2014, A&A, 566, A34
Kollmeier, J. A., Zasowski, G., Rix, H.-W., et al. 2017, arXiv:1711.03234
Kovačević, A. B., Radović, V., Ilić, D., et al. 2022, ApJS, 262, 49
Kozyreva, A., Nakar, E., Waldman, R., Blinnikov, S., & Baklanov, P. 2020, MNRAS, 494, 3927
Kromer, M., Fremling, C., Pakmor, R., et al. 2016, MNRAS, 459, 4428
Kruk, J. W., Xapsos, M. A., Armani, N., Stauffer, C., & Hirata, C. M. 2016, PASP, 128, 035005
Kulkarni, S. R., Harrison, F. A., Grefenstette, B. W., et al. 2021, arXiv:2111.15608
LaMassa, S. M., Cales, S., Moran, E. C., et al. 2015, ApJ, 800, 144
Langer, N. 2012, ARA&A, 50, 107
Lawrence, A. 2018, NatAs, 2, 102
Lawrence, A., Bruce, A. G., MacLeod, C., et al. 2016, MNRAS, 463, 296
Leloudas, G., Fraser, M., Stone, N. C., et al. 2016, NatAs, 1, 0002
Levinson, A., & Nakar, E. 2020, PhR, 866, 1
Li, J., McFadden, L. A., A'Hearn, M. F., et al. 2008, AAS/DPS Meeting, 40, 28.08
Lilly, S. J., Le Brun, V., Maier, C., et al. 2009, ApJS, 184, 218
Lim, G., Im, M., Paek, G. S. H., et al. 2023, ApJ, 949, 33
Lindegren, L., Klioner, S. A., Hernández, J., et al. 2021, A&A, 649, A2
Liran, T., Shvartzvald, Y., Lapid, O., et al. 2022, Proc. SPIE, 12181, 121812X
Livio, M., & Mazzali, P. 2018, PhR, 736, 1
Livio, M., Pringle, J. E., & Wood, K. 2005, ApJL, 632, L37
Loeb, A., & Maoz, D. 2013, MNRAS, 432, L11
Lu, W., Kumar, P., & Narayan, R. 2017, MNRAS, 468, 910
Luo, A. L., Zhao, Y. H., Zhao, G., et al. 2019, yCat, 5164, 0
MacLeod, C. L., Green, P. J., Anderson, S. F., et al. 2019, ApJ, 874, 8
Maeda, K., Jiang, J.-a., Shigeyama, T., & Doi, M. 2018, ApJ, 861, 78
Maeda, K., & Terada, Y. 2016, IJMPD, 25, 1630024
Magee, M. R., & Maguire, K. 2020, A&A, 642, A189
Magee, M. R., Maguire, K., Kotak, R., & Sim, S. A. 2021, MNRAS, 502, 3533
Malyali, A., Rau, A., Merloni, A., et al. 2021, A&A, 647, A9
Maoz, D., & Mannucci, F. 2012, PASA, 29, 447
Maoz, D., Mannucci, F., & Nelemans, G. 2014, ARA&A, 52, 107
Maoz, D., Mazeh, T., & McQuillan, A. 2015, MNRAS, 447, 1749
Maoz, D., & Rix, H.-W. 1993, ApJ, 416, 425
Margalit, B. 2022, ApJ, 933, 238
Margutti, R., & Chornock, R. 2021, ARA&A, 59, 155
Martin, D. C., Fanson, J., Schiminovich, D., et al. 2005, ApJL, 619, L1
Mason, K. O., Breeveld, A., Much, R., et al. 2001, A&A, 365, L36
McQuillan, A., Mazeh, T., & Aigrain, S. 2014, ApJS, 211, 24
Meadows, V., Reinhard, C., Arney, G., et al. 2018, AsBio, 18, 630
Merloni, A., Dwelly, T., Salvato, M., et al. 2015, MNRAS, 452, 69
Merloni, A., Predehl, P., Becker, W., et al. 2012, arXiv:1209.3114

Metzger, B. D., Thompson, T. A., & Quataert, E. 2018, ApJ, 856, 101
Meusinger, H., Hinze, A., & de Hoon, A. 2011, A&A, 525, A37
Miller, A. A., Cao, Y., Piro, A. L., et al. 2018, ApJ, 852, 100
Miller, A. A., Magee, M. R., Polin, A., et al. 2020, ApJ, 898, 56
Milne, P. A., Brown, P. J., Roming, P. W. A., Bufano, F., & Gehrels, N. 2013, ApJ, 779, 23
Minezaki, T., Yoshii, Y., Kobayashi, Y., et al. 2019, ApJ, 886, 150
Mockler, B., Guillochon, J., & Ramirez-Ruiz, E. 2019, ApJ, 872, 151
Mooley, K. P., Hallinan, G., Bourke, S., et al. 2016, ApJ, 818, 105
Morag, J., Sapir, N., & Waxman, E. 2022, MNRAS, 522, 2764
Moriya, T. J., Blinnikov, S. I., Tominaga, N., et al. 2013, MNRAS, 428, 1020
Mortsell, E., Goobar, A., Johansson, J., & Dhawan, S. 2022, ApJ, 935, 58
Nakar, E. 2020, PhR, 886, 1
Nakar, E., & Sari, R. 2010, ApJ, 725, 904
Nakar, E., & Sari, R. 2012, ApJ, 747, 88
Nedora, V., Bernuzzi, S., Radice, D., et al. 2021, ApJ, 906, 98
Netzer, H. 2022, MNRAS, 509, 2637
Neustadt, J. M. M., Holoien, T. W. S., Kochanek, C. S., et al. 2020, MNRAS, 494, 2538
Noebauer, U. M., Kromer, M., Taubenberger, S., et al. 2017, MNRAS, 472, 2787
Nordin, J., Aldering, G., Antilogus, P., et al. 2018, A&A, 614, A71
Nordin, J., Brinnel, V., van Santen, J., et al. 2019, A&A, 631, A147
Nugent, P. E., Sullivan, M., Cenko, S. B., et al. 2011, Natur, 480, 344
Ofek, E. O., 2014 MAAT: MATLAB Astronomy and Astrophysics Toolbox, Astrophysics Source Code Library, ascl:1407.005
Ofek, E. O., Arcavi, I., Tal, D., et al. 2014a, ApJ, 788, 154
Ofek, E. O., & Ben-Ami, S. 2020, PASP, 132, 125004
Ofek, E. O., Ben-Ami, S., Polishook, D., et al. 2023a, PASP, 135, 065001
Ofek, E. O., Rabinak, I., Neill, J. D., et al. 2010, ApJ, 724, 1396
Ofek, E. O., Rix, H.-W., & Maoz, D. 2003, MNRAS, 343, 639
Ofek, E. O., Shvartzvald, Y., Sharon, A., et al. 2023b, PASP, 135, 124502
Ofek, E. O., Sullivan, M., Shaviv, N. J., et al. 2014b, ApJ, 789, 104
Olling, R. P., Mushotzky, R., Shaya, E. J., et al. 2015, Natur, 521, 332
Olmedo, M., Chávez, M., Bertone, E., & De la Luz, V. 2013, PASP, 125, 1436
Page, M. J., Brindle, C., Talavera, A., et al. 2012, MNRAS, 426, 903
Pakmor, R., Kromer, M., Taubenberger, S., & Springel, V. 2013, ApJL, 770, L8
Pearson, J., Hosseinzadeh, G., Sand, D. J., et al. 2023, ApJ, 945, 107
Perego, A., Radice, D., & Bernuzzi, S. 2017, ApJL, 850, L37
Perego, A., Vescovi, D., Fiore, A., et al. 2022, ApJ, 925, 22
Perlmutter, S., Aldering, G., Goldhaber, G., et al. 1999, ApJ, 517, 565
Peterson, B. M. 1993, PASP, 105, 247
Phinney, E. S. 2009, arXiv:0903.0098
Pickles, A. J. 1998, PASP, 110, 863
Pinto, P. A., & Eastman, R. G. 2000, ApJ, 530, 757
Piro, A. L., Haynie, A., & Yao, Y. 2021, ApJ, 909, 209
Piro, A. L., & Kollmeier, J. A. 2018, ApJ, 855, 103
Piro, A. L., & Morozova, V. S. 2016, ApJ, 826, 96
Pizzocaro, D., Stelzer, B., Poretti, E., et al. 2019, A&A, 628, A41
Pognan, Q., Jerkstrand, A., & Grumer, J. 2022, MNRAS, 513, 5174
Pozo Nuñez, F., Bruckmann, C., Deesamutara, S., et al. 2023, MNRAS, 522, 2002
Quataert, E., & Shiode, J. 2012, MNRAS, 423, L92
Rabinak, I., & Waxman, E. 2011, ApJ, 728, 63
Radice, D., Bernuzzi, S., & Perego, A. 2020, ARNPS, 70, 95
Ramiaramanantsoa, T., Bowman, J. D., Shkolnik, E. L., et al. 2022, AN, 343, e10068
Ramolla, M., Haas, M., Westhues, C., et al. 2018, A&A, 620, A137
Ranjan, S., & Sasselov, D. D. 2016, AsBio, 16, 68
Rees, M. J. 1988, Natur, 333, 523
Rekhi, P., Ben-Ami, S., Perdelwitz, V., & Shvartzvald, Y. 2023, ApJ, 955, 24
Reusch, S., Stein, R., Kowalski, M., et al. 2022, PhRvL, 128, 221101
Rhoads, J. E. 1997, ApJL, 487, L1
Rhoads, J. E. 1999, ApJ, 525, 737
Richards, G. T., Croom, S. M., Anderson, S. F., et al. 2005, MNRAS, 360, 839
Ricker, G. R., Winn, J. N., Vanderspek, R., et al. 2015, JATIS, 1, 014003
Riess, A. G., Casertano, S., Yuan, W., Macri, L. M., & Scolnic, D. 2019, ApJ, 876, 85
Riess, A. G., Filippenko, A. V., Challis, P., et al. 1998, AJ, 116, 1009
Rigault, M., Copin, Y., Aldering, G., et al. 2013, A&A, 560, A66
Rigault, M., et al. 2015, ApJ, 802, 20
Rodrigues, X., Garrappa, S., Gao, S., et al. 2021, ApJ, 912, 54
Roettger, E. E., & Buratti, B. J. 1994, Icar, 112, 496
Rosswog, S., & Korobkin, O. 2022, AnP, 536, 2200306
Rosswog, S., Sollerman, J., Feindt, U., et al. 2018, A&A, 615, A132
Roth, N., Rossi, E. M., Krolik, J., et al. 2020, SSRv, 216, 114
Ruan, J. J., Anderson, S. F., Dexter, J., & Agol, E. 2014, ApJ, 783, 105
Rubin, A., Gal-Yam, A., De Cia, A., et al. 2016, ApJ, 820, 33
Rumbaugh, N., Shen, Y., Morganson, E., et al. 2018, ApJ, 854, 160
Runnoe, J. C., Cales, S., Ruan, J. J., et al. 2016, MNRAS, 455, 1691
Ryu, T., Krolik, J., & Piran, T. 2020, ApJ, 904, 73
Sagiv, I., Gal-Yam, A., Ofek, E. O., et al. 2014, AJ, 147, 79
Salz, M., Schneider, P. C., Fossati, L., et al. 2019, A&A, 623, A57
Sand, D. J., Brown, T., Haynes, R., & Dubberley, M. 2011, AAS Meeting, 218, 132.03
Sapir, N., Katz, B., & Waxman, E. 2013, ApJ, 774, 79
Sapir, N., & Waxman, E. 2017, ApJ, 838, 130
Sari, R., & Piran, T. 1999, ApJL, 517, L109
Sazonov, S., Gilfanov, M., Medvedev, P., et al. 2021, MNRAS, 508, 3820
Schawinski, K., Justham, S., Wolf, C., et al. 2008, Sci, 321, 223
Schlegel, D. J., Finkbeiner, D. P., & Davis, M. 1998, ApJ, 500, 525
Schulze, S., Malesani, D., Cucchiara, A., et al. 2014, A&A, 566, A102
Schutz, B. F. 1986, Natur, 323, 310
Seto, N., & Muto, T. 2011, MNRAS, 415, 3824
Shibata, M., & Hotokezaka, K. 2019, ARNPS, 69, 41
Siebert, M. R., Dimitriadis, G., Polin, A., & Foley, R. J. 2020, ApJL, 900, L27
Smartt, S. J. 2015, PASA, 32, e016
Smartt, S. J., Chen, T.-W., Jerkstrand, A., et al. 2017, Natur, 551, 75
Smith, K. L., Mushotzky, R. F., Boyd, P. T., et al. 2018, ApJ, 857, 141
Smith, N., & Arnett, W. D. 2014, ApJ, 785, 82
Soderberg, A. M., Berger, E., Page, K. L., et al. 2008, Natur, 453, 469
Soker, N. 2019, NewAR, 87, 101535
Soker, N., & Kashi, A. 2013, ApJL, 764, L6
Soumagnac, M. T., Ganot, N., Irani, I., et al. 2020a, ApJ, 902, 6
Soumagnac, M. T., Ofek, E. O., Gal-yam, A., et al. 2019, ApJ, 872, 141
Soumagnac, M. T., Ofek, E. O., Liang, J., et al. 2020b, ApJ, 899, 51
Springer, O. M., & Ofek, E. O. 2021a, MNRAS, 506, 864
Springer, O. M., & Ofek, E. O. 2021b, MNRAS, 508, 3166
Stassun, K. G., Oelkers, R. J., & Paegert, M. 2019, AJ, 158, 138
Steeghs, D., Galloway, D. K., Ackley, K., et al. 2022, MNRAS, 511, 2405
Stein, R., Velzen, S. v., Kowalski, M., et al. 2021, NatAs, 5, 510
Stern, D., McKernan, B., Graham, M. J., et al. 2018, ApJ, 864, 27
Stone, N., & Loeb, A. 2011, MNRAS, 412, 75
Stone, N., & Loeb, A. 2012, PhRvL, 108, 061302
Stone, N. C., & Metzger, B. D. 2016, MNRAS, 455, 859
Strotjohann, N. L., Ofek, E. O., Gal-Yam, A., et al. 2021, ApJ, 907, 99
Suárez Mascareño, A., Rebolo, R., & González Hernández, J. I. 2016, A&A, 595, A12
Suárez-Madrigal, A., Krumholz, M., & Ramirez-Ruiz, E. 2013, arXiv:1304.2317
Tal-Or, L., Zechmeister, M., Reiners, A., et al. 2018, A&A, 614, A122
Tan, J. C., Matzner, C. D., & McKee, C. F. 2001, ApJ, 551, 946
Tanaka, M., Utsumi, Y., Mazzali, P. A., et al. 2017, PASJ, 69, 102
Teplitz, H. I., Rafelski, M., Kurczynski, P., et al. 2013, AJ, 146, 159
The LSST Dark Energy Science Collaboration, Mandelbaum, R., & Eifler, T. 2018, arXiv:1809.01669
Trakhtenbrot, B., Arcavi, I., MacLeod, C. L., et al. 2019a, ApJ, 883, 94
Trakhtenbrot, B., Arcavi, I., Ricci, C., et al. 2019b, NatAs, 3, 242
Trakhtenbrot, B., & Netzer, H. 2012, MNRAS, 427, 3081
Treu, T., & Marshall, P. J. 2016, A&ARv, 24, 11
Tumlinson, J., Peeples, M. S., & Werk, J. K. 2017, ARA&A, 55, 389
van Sluijs, L., & Van Eylen, V. 2018, MNRAS, 474, 4603
van Velzen, S. 2018, ApJ, 852, 72
van Velzen, S., Farrar, G. R., Gezari, S., et al. 2011, ApJ, 741, 73
van Velzen, S., Gezari, S., Hammerstein, E., et al. 2021, ApJ, 908, 4
van Velzen, S., Holoien, T. W. S., Onori, F., Hung, T., & Arcavi, I. 2020, SSRv, 216, 124
Vanden Berk, D. E., Richards, G. T., Bauer, A., et al. 2001, AJ, 122, 549
Vanden Berk, D. E., Wilhite, B. C., Kron, R. G., et al. 2004, ApJ, 601, 692
Vanderburg, A., Rappaport, S. A., Xu, S., et al. 2020, Natur, 585, 363
Vedantham, H. K., Callingham, J. R., Shimwell, T. W., et al. 2020, NatAs, 4, 577
Veefkind, J., Aben, I., McMullan, K., et al. 2012, RSEnv, 120, 70
Veras, D. 2021, Oxford Research Encyclopedia of Planetary Science (Oxford: Oxford Univ. Press), 1
Vidal-Madjar, A., Huitson, C. M., Bourrier, V., et al. 2013, A&A, 560, A54
Villadsen, J., & Hallinan, G. 2019, ApJ, 871, 214
Vincentelli, F. M., McHardy, I., Cackett, E. M., et al. 2021, MNRAS, 504, 4337
Wang, J., & Merritt, D. 2004, ApJ, 600, 149
Wasleske, E. J., Baldassare, V. F., & Carroll, C. M. 2022, ApJ, 933, 37

Waszczak, A., Ofek, E. O., & Kulkarni, S. R. 2015, ApJ, 809, 92
Watson, D., Hansen, C. J., Selsing, J., et al. 2019, Natur, 574, 497
Waxman, E., & Katz, B. 2017, in Handbook of Supernovae, ed. A. W. Alsabti & P. Murdin (Berlin: Springer), 967
Waxman, E., Mészáros, P., & Campana, S. 2007, ApJ, 667, 351
Waxman, E., Ofek, E. O., Kushnir, D., & Gal-Yam, A. 2018, MNRAS, 481, 3423
Weaver, J. R., Kauffmann, O. B., Ilbert, O., et al. 2022, ApJS, 258, 11
Wen, S., Jonker, P. G., Stone, N. C., Zabludoff, A. I., & Psaltis, D. 2020, ApJ, 897, 80
Wen, S., Jonker, P. G., Stone, N. C., & Zabludoff, A. I. 2021, ApJ, 918, 46
Werner, N., Řípa, J., Münz, F., et al. 2022, Proc. SPIE, 12181, 121810B
Wilhite, B. C., Brunner, R. J., Grier, C. J., Schneider, D. P., & vanden Berk, D. E. 2008, MNRAS, 383, 1232
Wilson, D. J., Gänsicke, B. T., Koester, D., et al. 2019, MNRAS, 483, 2941
Wilson, D. J., Hermes, J. J., & Gänsicke, B. T. 2020, ApJL, 897, L31
Winn, J. N., & Fabrycky, D. C. 2015, ARA&A, 53, 409
Wong, K. C., Suyu, S. H., Chen, G. C. F., et al. 2020, MNRAS, 498, 1420
Woosley, S. E., Blinnikov, S., & Heger, A. 2007, Natur, 450, 390
Woosley, S. E., Heger, A., & Weaver, T. A. 2002, RvMP, 74, 1015
Wright, N. J., Drake, J. J., Mamajek, E. E., & Henry, G. W. 2011, ApJ, 743, 48
Xu, C. K., Donas, J., Arnouts, S., et al. 2005, ApJL, 619, L11
Xu, S., Hallakoun, N., Gary, B., et al. 2019, AJ, 157, 255
Yao, Y., Ravi, V., Gezari, S., et al. 2023, ApJL, 955, L6
Yu, Z., Martini, P., Penton, A., et al. 2023, MNRAS, 522, 4132
Zeltyn, G., Trakhtenbrot, B., Eracleous, M., et al. 2022, ApJL, 939, L16
Zimmerman, E. A., Irani, I., Chen, P., et al. 2023, arXiv:2310.10727
Zu, Y., Kochanek, C. S., Kozłowski, S., & Peterson, B. M. 2016, ApJ, 819, 122
Zuckerman, B., Koester, D., Reid, I. N., & Hünsch, M. 2003, ApJ, 596, 477
Zuckerman, B., Melis, C., Klein, B., Koester, D., & Jura, M. 2010, ApJ, 722, 725